ELSEVIER

Precambrian Research 117 (2002) 57–84

Precambrian Research

www.elsevier.com/locate/precamres

Late Eburnean granitization and tectonics along the western and northwestern margin of the Archean Kénéma–Man domain (Guinea, West African Craton)

Emmanuel Egal [a,*], Denis Thiéblemont [a], Didier Lahondère [a], Catherine Guerrot [a], Cristian Adi Costea [b], Dan Iliescu [b], Claude Delor [a], Jean-Christian Goujou [c], Jean Michel Lafon [d], Monique Tegyey [a], Sory Diaby [e], Pascal Kolié [e]

[a] *BRGM, BP 6009, 3, avenue C. Guillemin, 45060 Orleans Cedex 2, France*
[b] *PROSPECTIUNI S.A., 1 Caransebes Street, Sector 1, Bucharest 78344, Romania*
[c] *JCG Consult, Les Grands Goulets, 26420 La Chapelle-en-Vercors, France*
[d] *Isotope Geology Laboratory Geosciences Center, Federal University of Para, Belem, Brazil*
[e] *DNRGH, BP 295, Conakry, Guinea*

Received 12 July 2001; accepted 2 May 2002

Abstract

Recent mapping of the eastern part of Guinea has revealed a vast plutonic belt that rims the margin of the Archean Kénéma–Man craton and that is made up of a variety of granitic rocks (granodiorite, biotite granite, monzogranite, two-mica granite), granodiorite, with common clinopyroxene, being the most abundant. Single-zircon dating by stepwise Pb-evaporation carried out on characteristic rock types (granodiorite, monzogranite, two-mica granite) reveals their age to be late Eburnean (c. 2090–2070 Ma), and indicates that their emplacement occurred within a relatively short time interval ($\leqslant$ 20 Ma). The granodiorite, biotite granite and monzogranite of the plutonic belt all present a calc-alkaline and highly potassic nature and show numerous analogies with the Neogene calc-alkaline rocks of the central Andes; there is evidence to suggest strong contamination from the Archean crust. These analogies make it possible to envisage the emplacement of the plutonic belt directly above a subduction zone. The occurrence of peraluminous two-mica granite at the northern extension of the plutonic belt in the Siguiri Basin may suggest that the convergence here was associated with the local melting of metasedimentary rocks in the deep part of the basin. Contemporaneously with its emplacement, the late Eburnean plutonic belt accommodated regional convergence by major WNW–ESE sinistral movements along the northwestern margin of the Archean block. Horizontal shortening towards the WSW is envisaged at the scale of eastern Guinea in relation with these kinematics. The late Eburnean plutonic belt of eastern Guinea is a key element of the Archean/Proterozoic transition zone in the southern part of West Africa. Evidence along the western and northwestern border of the Archean Kénéma–Man domain leads us to

* Corresponding author. Fax: +33-2-38643685
E-mail address: e.egal@brgm.fr (E. Egal).

0301-9268/02/$ - see front matter
PII: S0301-9268(02)00060-8

interpret this transition zone as an active margin, along which strike–slip tectonism accommodated regional convergence towards the end of the Eburnean cycle. © 2002 Published by Elsevier Science B.V.

Keywords: Paleoproterozoic; West African Craton; Pb/Pb single-zircon dating; Active margin; Strike–slip tectonism; Eastern Guinea

1. Introduction

The southern part of the West African Craton (or Leo Rise) comprises two distinct entities (Bessoles, 1977; Cahen et al., 1984) (Fig. 1), namely the Archean Kénéma–Man domain making up the southwestern part of the craton, and the Paleoproterozoic Baoulé-Mossi domain (Birimian domain in the broad sense of the term) forming the central and eastern parts. The Archean domain shows the superposition of at least two major tectono-magmatic cycles (MacFarlane et al., 1981; Beckinsale et al., 1980; Camil et al., 1983; Kouamelan et al., 1997): the Leonian (~ 2900–3000 Ma) and Liberian (~ 2700–2800 Ma) cycles. The Paleoproterozoic or Birimian domain, however, was established and structured during a single cycle, the Eburnean (~ 2200–2000 Ma). The term 'Eburnean' refers to all tectonic, metamorphic and plutonic events affecting the Birimian rocks during the Paleoproterozoic at about 2200–2000 Ma (Bonhomme, 1962). No determining evidence exists to suggest the presence of an Archean basement under the Paleoproterozoic domain (Milési et al., 1989; Abouchami et al., 1990; Boher et al., 1992; Hirdes et al., 1992).

The boundary between the Archean and Paleoproterozoic domains (Fig. 1) is traditionally identified as the Sassandra Fault in the southern part of the craton and, less precisely, as the

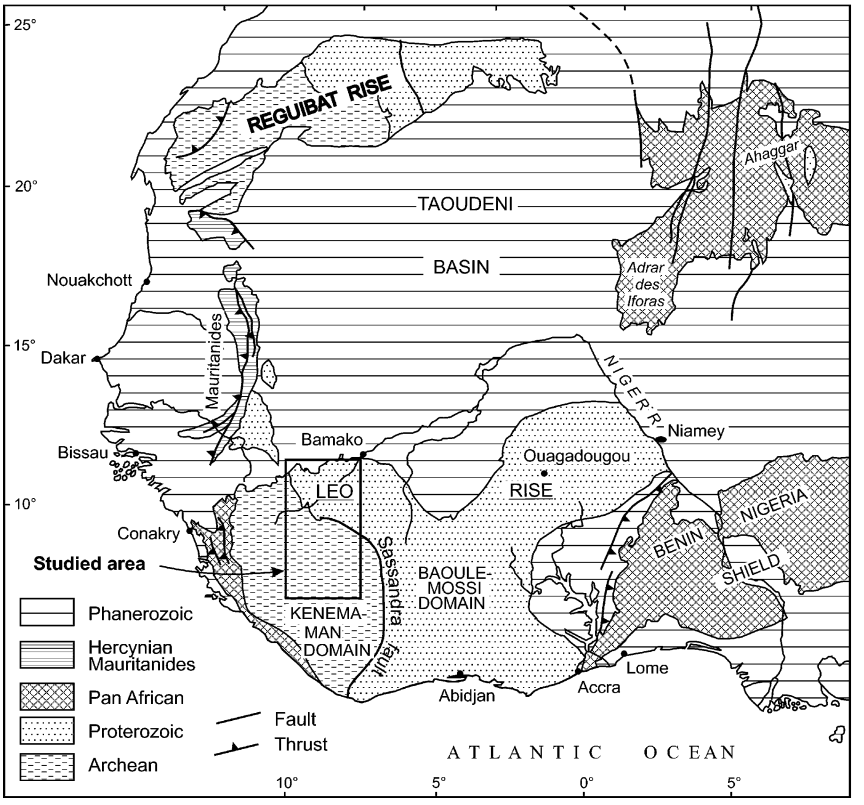

Fig. 1. Geological sketch map of the West African Craton showing the location of the studied area (adapted from Fig. 1 in Boher et al., 1992).

southern boundary of the Birimian basin of Upper Guinea (Siguiri Basin) in the northern part. Nonetheless, recent work undertaken in the Ivory Coast (Kouamelan et al., 1997) and southeastern Guinea (Billa et al., 1999) has revealed an extension of Paleoproterozoic (Eburnean) tectonism and granitization into the actual Archean domain. The nature of this Archean/Proterozoic transition zone is still under widespread debate (Feybesse and Milèsi, 1994), and the commonly 'old' mapping work (e.g. Obermüller, 1941, and Goloubinow, 1936, for eastern Guinea) leaves room for a fairly wide range of interpretation.

A mapping survey at the 1:200 000 scale has been recently undertaken in eastern Guinea (12 map sheets published in 1999 by the Guinean Ministry of Mines, Geology and the Environment[1]), covering the northern and eastern margins of the Archean Shield and the Siguiri Basin. The results of this new mapping work, backed up by accurate geochemical and geochronological data, have notably led to the identification of a localized Paleoproterozoic plutonic belt around the Archean craton. The characteristics and age of this belt, as well as its tectonic deformation, are presented in this paper. These data have led us to propose a new geodynamic interpretation for the transition zone between the Archean and Paleoproterozoic blocks in southwest Africa.

2. Geological framework of eastern Guinea

Eastern Guinea is made up predominantly of Precambrian rocks (Fig. 2). The most recent formations are represented, in the far north, by Neoproterozoic sediments of the southern limit of the Taoudéni Basin (Fig. 1) and by scattered traps and dykes of Early Jurassic dolerite and gabbro associated with the opening of the central Atlantic (Deckart et al., 1997).

[1] Distribution and sales: Centre de Promotion et de développement Miniers (*Center for Mining Promotion and Development*)—CPDM—BP 295, Conakry, Republic of Guinea. Tel.: +224-41-15-44; fax: +224-41-49-13.

Three main entities are distinguished within the Precambrian (Figs. 2 and 3): (1) an Archean gneissic and granitic domain with supracrustal intercalations, within which are identified two banded iron formation (BIF) ranges (Simandou and Nimba) and some restricted plutons of Paleoproterozoic age; (2) a Paleoproterozoic basin (Siguiri Basin) extending northeastward towards Mali; (3) a plutonic belt, identified during recent geological mapping and presented in this paper, made up of various Paleoproterozoic granitic rocks, surrounding the Archean domain and in contact with the Siguiri Basin.

2.1. The Archean domain

The Archean was first mapped by Obermüller (1941). The recent mapping work has enabled the previous interpretations to be clarified, and three new units are now distinguished (Fig. 2).

(1) A pre-Liberian (i.e. older than 2.8–2.9 Ga), high grade metamorphic succession (amphibolite to granulite facies), partially affected by retrograde metamorphism. An age of 3050 ± 16 Ma has been obtained on zircons (SHRIMP) from an orthogneiss (Goujou et al., 1999). Within the succession, along the western foothills of Mount Nimba, the recent mapping has revealed a specific granite–gneiss unit (Fig. 2): a geochronological investigation using SHRIMP on zircons has revealed emplacement ages of 3542 ± 13 Ma (Thiéblemont et al., 2001); this unit thus constitutes the first evidence of an Early Archean basement in the Leo Rise.

(2) Two batholiths of Liberian age ($\sim$2800–2900 Ma) (Bering et al., 1998; Goujou et al., 1999; Thiéblemont et al., 2001) occupy the western and southeastern parts of the Guinean forest region. Towards the southwest in Liberia, the western batholith gives way to a batholith imprecisely dated at some 2650 Ma (Hurley et al., 1971), whereas towards the east, the southeastern batholith gives way to granitic rocks of the Man domain (Ivory Coast) dated at about 2800 Ma (Camil et al., 1983; Kouamelan et al., 1997; Cocherie et al., 1998).

(3) Two 'BIF' units, the Nimba and Simandou successions (Lamotte and Routhier, 1943; Ober-

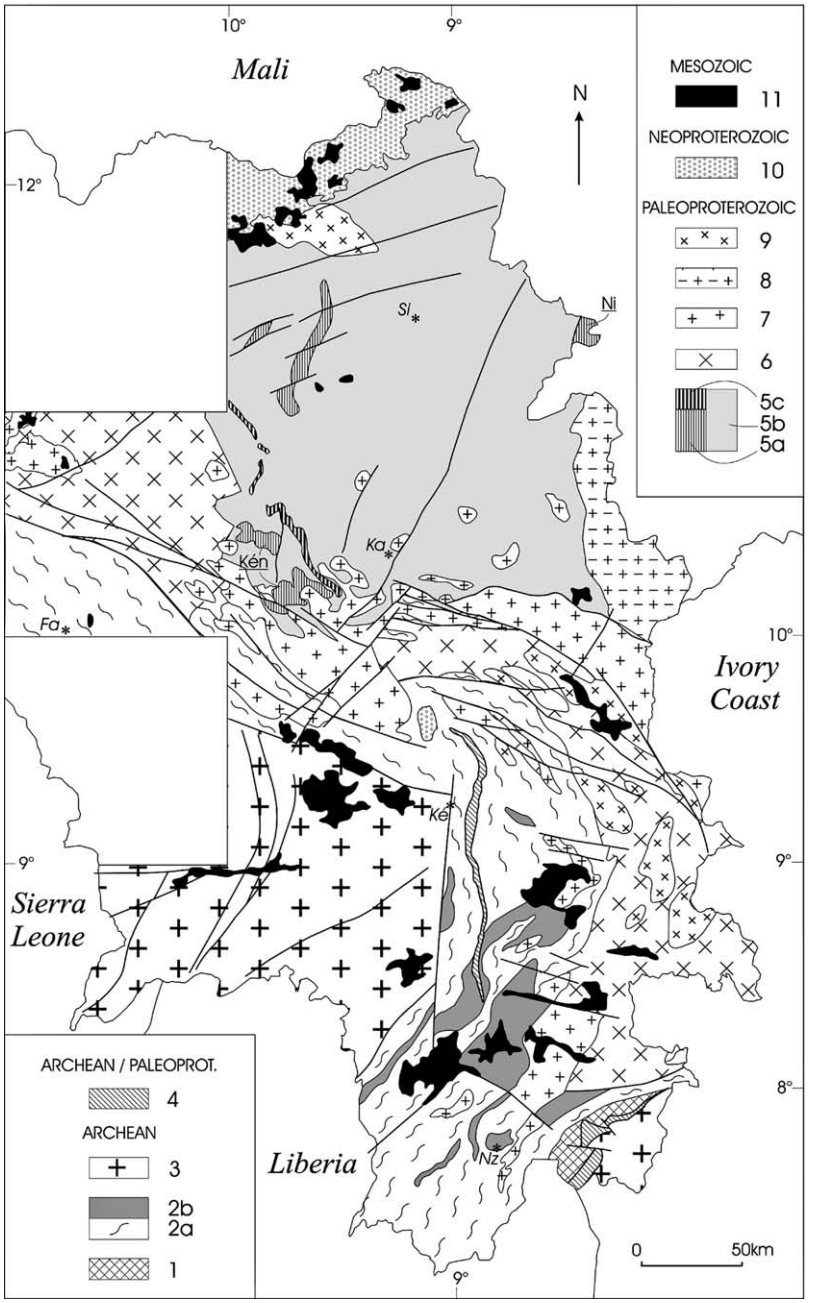

Fig. 2. Geological map of eastern Guinea compiled after the recent 1:200 000-scale mapping survey. The white square areas within Guinea were not documented during the survey. 1–Early Archean orthogneiss (~3540 Ma). 2–Middle Archean gneiss and migmatite (a) and amphibolite (b) (~3200–3000 Ma). 3–Liberian granitic rocks (2900–2800 Ma). 4–BIF of late Archean/Early Proterozoic age. 5–Low-grade metamorphic sediments and volcanics of the Birimian Siguiri Basin: (a) acid to intermediate (locally basic) volcanic rocks (Ni, Niani complex dated at ~2210 Ma; Kén, Kéniéro complex dated at ~2095 Ma); (b) detrital sedimentary rocks (mainly argilite and sandstone); (c) komatiitic volcanics of the Niandan succession. 6–Late Eburnean granodiorite (~2090–2070 Ma). 7–Late Eburnean biotite granite. 8–Late Eburnean two-mica granite (~2080 Ma). 9–Late Eburnean monzogranite (~2075 Ma). 10–Neoproterozoic sediments of the Taoudeni Basin. 11–Early Jurassic dolerite and gabbro. Fa, Faranah; Ka, Kankan; Ké, Kérouané; Nz, Nzérékoré; Si, Siguiri.

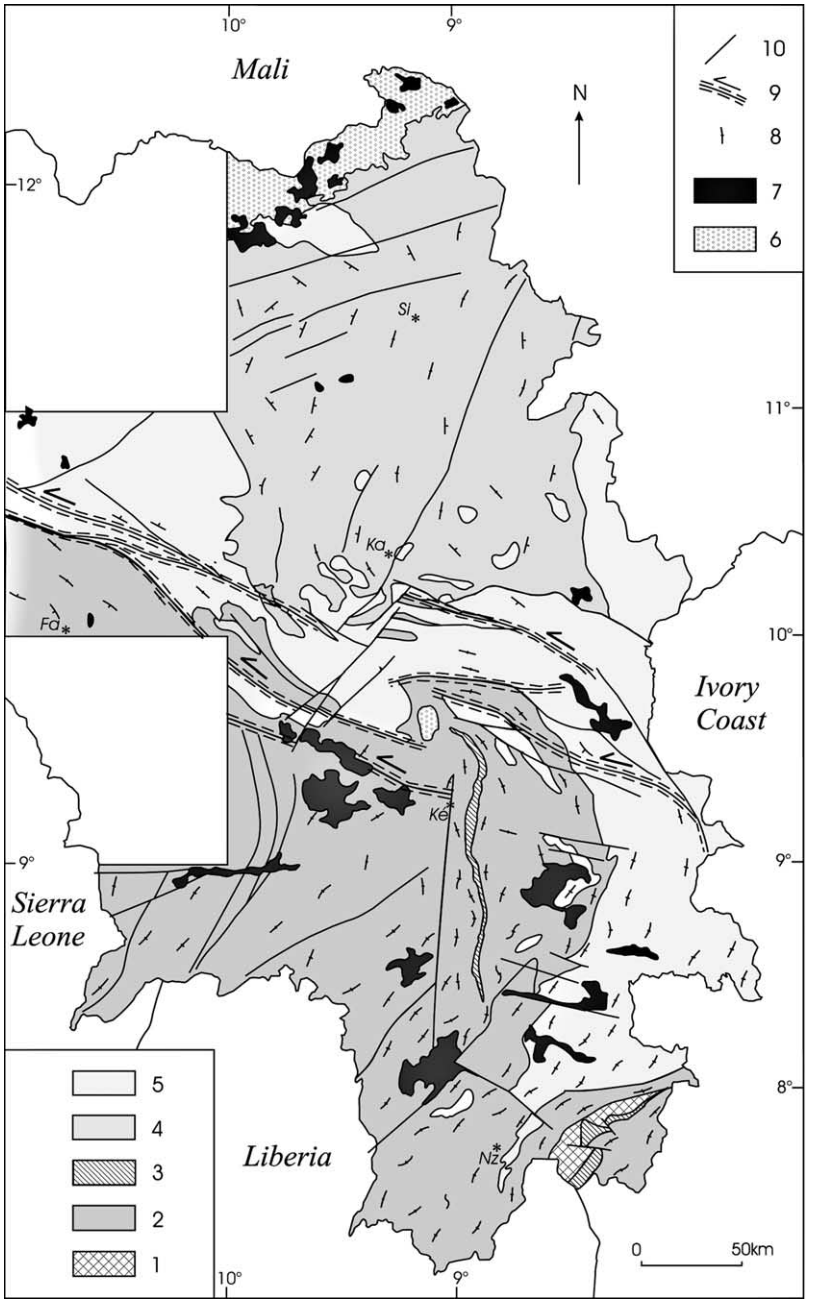

Fig. 3. Simplified geological and structural map of eastern Guinea. 1–Early Archean orthogneiss (~ 3540 Ma). 2–Middle to late Archean formations (~ 3200–2800 Ma). 3–BIF of late Archean/Early Proterozoic age. 4–Metasediments and metavolcanics of the Early Proterozoic (Birimian) Siguiri Basin. 5–Late Eburnean granitic rocks (~ 2090–2070 Ma). 6–Neoproterozoic sediments of the Taoudeni Basin. 7–Early Jurassic dolerite and gabbro. 8–Major foliation within Archean and Proterozoic rocks. 9–Major sinistral ductile shear zones. 10–Other shear zones and faults. Fa, Faranah; Ka, Kankan; Ké, Kérouané; Nz, Nzérékoré; Si, Siguiri.

müller and Roques, 1946), whose unconformable relationship over the Archean gneiss and granitic rocks has been confirmed (Obermüller, 1941; Billa et al., 1999; Lahondère et al., 1999). These two ranges, made up essentially of metavolcanic and metasedimentary (mainly banded ferriferous quartzite) rocks, are now attributed to the late Archean/Early Proterozoic on the basis of maximum ages obtained on detrital zircons extracted from quartzite, i.e. 2615 Ma for the Nimba succession (Billa et al., 1999) and 2711–2871 Ma for the Simandou succession (Thiéblemont et al., 1999).

2.2. The Birimian Siguiri Basin

The Siguiri Basin occupies a vast area in the northern part of eastern Guinea (Figs. 1 and 2). It disappears to the north beneath Neoproterozoic sediments of the Taoudéni Basin. Elsewhere, the basin is bounded by intrusive granitic rocks belonging to the plutonic belt presented in this paper. Along the southern edge of the basin, granitic–gneissic rocks assigned to the Archean are exposed in local tectonic thrust slices.

The Siguiri Basin is essentially composed of marine detrital sedimentary rocks (argilite to fine-grained sandstones) and, to a lesser degree, volcanic rocks (lava and pyroclastics) intercalated within these sediments, and subvolcanic dykes. All the rocks show irregular foliation and generally weak metamorphism; sericite is ubiquitous. Locally, the sediments are transformed into mica schist, at least partially due to 'thermal' metamorphism at the contact of the neighbouring plutons. This is the case, for instance, around the monzogranitic pluton cropping out within the northern part of the basin. Along the southern edge of the basin, mica schist containing staurolite, sillimanite and garnet is fairly well developed.

Several volcanic units of cartographic scale are distinguished (Fig. 2). Geochronological and geochemical results have been obtained from these units. The Niani complex, composed of a variety of volcanic rocks, crops out in the eastern part of the basin near the border with Mali. Its emplacement is dated at 2211 ± 3 Ma (Lahondère et al., in press-a, Lahondère et al., in press-b), which is the oldest age obtained from zircons in the Paleoproterozoic of West Africa. All the rocks show geochemical similarities with lava from present-day subduction zones (Lahondère et al., in press-a, Lahondère et al., in press-b). The volcanic range of Kéniéro crops out at the southwestern limit of the Siguiri Basin. It is also made up of a group of various volcanics, but is clearly younger than the Niani complex: a rhyolite was dated at 2093 ± 2 Ma (Feybesse et al., 1999).

2.3. The plutonic belt

The plutonic belt forms a large batholith composed of various granitic rocks and extends along the edge of the Archean craton, separating it from the Siguiri Basin further to the northwest (Figs. 2 and 3). The belt, with an average width of 50–100 km, globally strikes SE–NW in the north, becoming E–W around 10°N and N–S to the south of 9°30′N, before dying out at 8°N. Some isolated plutons crop out within the Siguiri Basin and the Archean domain.

The characteristics of this plutonic belt are presented and discussed in the following sections.

3. Lithology of the plutonic belt

The most common rock type of the plutonic belt is granodiorite, which constitutes a vast batholith that cuts the small granite plutons and veins. In the northwest and along the southern edge of the Siguiri Basin, these plutons are essentially composed of biotite granite. The biotite granite is present within the actual basin, the eastern limit of which is marked by a huge pluton of two-mica granite. Towards the south and also within the Siguiri Basin, the granodioritic batholith is cut by small plutons and veins of leucocratic monzogranite rich in potassic feldspar. Granodiorite and monzogranite coexist all along the eastern margin of the Archean craton southwards down to 8°N.

The biotite granite cuts the granodiorite, but both are sheared by regional major strike–slip

faults (Section 6). Monzogranite commonly contains granodiorite enclaves and locally forms veins that cut the granodiorite: in certain cases, these veins cut the sheared granodiorite. No relationship has been observed in the field between the two-mica granite and the other granitic rocks of the belt.

3.1. Granodiorite

The granodiorite is the dominant rock type within the belt, cropping out almost continuously between 8°N and 11°N. Its texture is granular to porphyroid (potassic feldspar phenocrysts), equant to clearly oriented, and even mylonitic to ultramylonitic in places. Locally, the granodiorite evolves towards tonalite, diorite or syenite through variations in the proportion of potassic feldspar and ferro-magnesian minerals. Mafic minerals include biotite, amphibole and clinopyroxene (orthopyroxene is nowhere observed), and their distribution varies depending on the area. In the northwestern and central parts, the main type is a light granodiorite with biotite and amphibole (magnesian hornblende), within which clinopyroxene (augite–salite) exists locally as relics in the cores of large amphiboles. However, towards the southeast, clinopyroxene is abundant, clearly visible to the naked eye and generally very fresh, although it can be partially recrystallized into amphibole and/or biotite. Sphene is the main accessory mineral.

Dark enclaves are randomly distributed within the granodiorite and are highly abundant in places. They mainly consist of amphibole gneiss, amphibolite and amphibolo-pyroxenite, although biotite gneiss is also observed locally.

In the zones with little or no deformation, the granodiorite shows magmatic flow banding marked by the arrangement of enclaves and feldspar phenocrysts along a generally almost vertical plane. The enclaves are elongate, segmented and commonly show asymmetric shapes compatible with a flow of the material in a sub-southwards direction. Locally, the rocks show mylonitic deformation marking major sinistral strike–slip faults, which will be described later.

3.2. Biotite granite

Numerous intrusions are assigned to the biotite granite rock type in the central and western part of the belt (Fig. 2).

The actual rock, of mainly granitic composition, shows a variable texture and grain size: some plutons clearly exhibit an association of porphyroid, medium-coarse and fine-grained (latest) rocks, as well as pegmatite veins. Enclaves of basic rock and gneiss (Archean?) are observed in places.

The main granitic paragenesis is composed of potassic feldspar (microcline) and plagioclase (oligoclase) in equivalent proportions, and of quartz and brown biotite. Sphene is relatively abundant. Random zircon is present, nowhere in abundance, and generally in small altered crystals.

The granite is either equant to slightly oriented (discreet magmatic fabric), or shows a marked and commonly visible foliation, especially near the major shear zones.

In the southern part of the Siguiri Basin, the biotite granites are cartographically grouped with intercalated staurolite-, garnet- and sillimanite-bearing mica schist (metapelite) recognized in this area. The mica schist underwent migmatization to varying degrees, in places corresponding to true metatexite. The observations lead us to believe that this 'granite–migmatite complex' is made up of metasediments widely intruded and partially melted by widespread biotite granite bodies.

3.3. Monzogranite

A few small intrusions of monzogranite are located in the eastern and southeastern part of the plutonic belt. A larger pluton crops out in the northern part of the Siguiri Basin.

The monzogranite is leucocratic, equant, fine to coarse grained, in places porphyroid and exceptionally deformed. It forms bodies extending from a few kilometres to tens of kilometres within pyroxene-bearing granodiorite or within the metasediments of the Siguiri Basin (Fig. 2).

The monzogranite is made up of microcline (abundant), plagioclase (scarce), quartz and biotite, as small variably chloritized lamellae. Acces-

sory minerals, namely zircon, monazite and apatite, are particularly scarce.

3.4. Two-mica granite

Two-mica granite crops out over a limited area slightly set aside from the main part of the plutonic belt, to the east of the Siguiri Basin, near the border with the Ivory Coast where its extent is unknown. The granite is undeformed at the few outcrops visited. The rock has an equant granular texture of medium grain size and is composed of plagioclase (oligoclase) and potassic feldspar (microcline) in equivalent proportions, interstitial quartz (or myrmekite), muscovite and biotite. Accessory minerals are represented by apatite (as large crystals or needles), zircon and rutile (needles) within the biotite lamellae.

4. Geochronology of the plutonic belt

4.1. Analytical procedures

Of the six datings reported in this paper obtained using the direct lead evaporation method (TIMS—Pb evaporation analyses), five were carried out at BRGM, and one (BEY-1103) at the Geochronological Laboratory of the Federal University of Pará, (Belém, Brazil).

At BRGM, the radiometric dating was carried out using the zircon evaporation technique (Kober, 1986, 1987) according to the detailed technical procedure described in Cocherie et al. (1992). Isotope measurements were performed on a Finnigan MAT 261 mass spectrometer in dynamic mode, using a secondary electron multiplier. Common Pb corrections were done according to Stacey and Kramers (1975). The average $^{207}Pb^*/^{206}Pb^*$ age for all steps is given to $\pm 1\sigma$ one standard deviation on all $^{207}Pb^*/^{206}Pb^*$ individual ratios). Similarly, when several steps are recorded for a given grain, a 'zircon age' is obtained with $\pm 1\sigma$ one standard deviation calculated with all corresponding recorded $^{207}Pb^*/^{206}Pb^*$ ages. Finally, if several zircons give over various steps the same age within the analytical uncertainties, a weighted average age, based on all individual steps, is calculated with $\pm 2\sigma$ (95% confidence limit) using the ISOPLOT/EX program from Ludwig (1999). This method usually leads to a lower uncertainty than a simple average of ages corresponding to all individual $^{207}Pb^*/^{206}Pb^*$ ratios with 1σ (Cocherie et al., 1992). However, its main advantage is that it takes better account of the uncertainty on each step age with this weighted procedure, also adopted by Klötzli (1997). The analytical results are given in Table 1.

The single-grain Pb evaporation analyses made at Belém also followed the method of Kober (1986, 1987). Isotope analyses were carried out on a Finnigan MAT262 mass spectrometer in dynamic mode using an ion counting detector. $^{207}Pb/^{206}Pb$ ratios were corrected for mass fractionation with a factor of $0.12\% \pm 0.03$ per mass unit, determined by repeated analyses of the NBS-982 lead standard. Analyses with $^{206}Pb/^{204}Pb$ ratios lower than 2500 were eliminated. Common Pb corrections were done using the Stacey and Kramers (1975) model. Weighted mean and errors on the $^{207}Pb/^{206}Pb$ ages were calculated according to Gaudette et al. (1998). The analytical results are given in Table 2 (2σ level).

4.2. Geochronological results

The datings presented hereafter are plotted on Fig. 4, which also shows the location of the dated samples.

4.2.1. Granodiorite

Three samples were dated at BRGM Orléans: a granodiorite with amphibole and biotite (ID510), a granodiorite with amphibole (DL378), and a diorite (DL169A). A pyroxene-bearing granodiorite (BEY1103) was dated at Belém.

Of the seven zircons selected from sample ID510, only three (A, C, F) gave a stable Pb signal. Six consecutive steps were obtained for zircon F, and two or one for zircons A and C (Table 1). The ages are coherent, and the age obtained on the single zircon F shows a high precision (2075 ± 8 Ma). The weighted mean age calculated for all the measurements is 2072 ± 4 Ma (2σ) (Fig. 5a), which is considered as the age of crystallization of granodiorite ID510.

Table 1
Analytical data obtained through lead evaporation on single zircons at BRGM

Sample	Zircon	T (°C)	Number of ratios	$^{206}Pb/^{204}Pb$	$^{208}Pb/^{206}Pb$	$^{207}Pb^*/^{206}Pb^* \pm 1\sigma$	Step age $\pm 1\sigma$	Zircon age $\pm 1\sigma$	Mean age $\pm 2\sigma$
ID510	Zr A	**1480**	**37**	**7055**	**0.104**	**0.12773 ± 66**	**2067 ± 9**		**2072 ± 4**
		1500	**40**	**4495**	**0.133**	**0.12744 ± 44**	**2063 ± 6**	**2065 ± 8**	**MSWD = 1.19**
	Zr C	**1500**	**28**	**5000**	**0.121**	**0.12759 ± 36**	**2065 ± 5**	**2065 ± 5**	**(9 steps)**
	Zr F	**1500**	**21**	**7630**	**0.139**	**0.12781 ± 87**	**2068 ± 12**		
		1520	**17**	**17 950**	**0.136**	**0.12875 ± 44**	**2081 ± 6**		
		1560	**34**	**5805**	**0.125**	**0.12795 ± 88**	**2070 ± 12**		
		1600	**68**	**10 325**	**0.112**	**0.12810 ± 58**	**2072 ± 8**	**2075 ± 8**	
		1640	**87**	**12 040**	**0.113**	**0.12839 ± 36**	**2076 ± 5**		
		1680	**61**	**17 740**	**0.137**	**0.12861 ± 36**	**2079 ± 5**		
DL378	Zr A	1480	23	1770	0.217	0.12209 ± 90	1987 ± 13		2081 ± 4
	Zr B	**1480**	**23**	**11 380**	**0.140**	**0.12836 ± 66**	**2076 ± 9**	**2076 ± 9**	**MSWD = 1.40**
	Zr C	**1480**	**69**	**15 215**	**0.112**	**0.12810 ± 44**	**2072 ± 6**		**(12 steps)**
		1500	**62**	**16 670**	**0.129**	**0.12827 ± 52**	**2074 ± 7**		
		1520	**13**	**9120**	**0.145**	**0.12863 ± 59**	**2079 ± 8**		
		1560	**60**	**14 715**	**0.116**	**0.12863 ± 56**	**2079 ± 8**	**2080 ± 9**	
		1600	**59**	**14 820**	**0.113**	**0.12912 ± 46**	**2086 ± 6**		
		1680	**64**	**13 025**	**0.129**	**0.12932 ± 23**	**2089 ± 3**		
	Zr D	**1480**	**69**	**22 120**	**0.078**	**0.12823 ± 30**	**2074 ± 4**		
		1500	**54**	**18 240**	**0.073**	**0.12837 ± 68**	**2076 ± 9**		
		1520	**70**	**34 890**	**0.077**	**0.12883 ± 43**	**2082 ± 6**	**2078 ± 8**	
		1580	**41**	**8200**	**0.080**	**0.12887 ± 69**	**2083 ± 9**		
	Zr E	**1500**	**42**	**2165**	**0.237**	**0.12886 ± 62**	**2083 ± 8**	**2083 ± 8**	
DL169A	Zr A	**1480**	**20**	**11 570**	**0.149**	**0.12807 ± 94**	**2072 ± 13**	**2072 ± 13**	**2074 ± 8**
	Zr B	1480	7	10 240	0.163	0.12781 ± 279	2068 ± 38		MSWD = 0.15
		1500	**15**	**4715**	**0.136**	**0.12853 ± 82**	**2078 ± 11**	**2078 ± 11**	**(7 steps)**
	Zr C	**1480**	**47**	**8800**	**0.112**	**0.12859 ± 86**	**2079 ± 12**		
		1500	**25**	**8160**	**0.110**	**0.12835 ± 87**	**2076 ± 12**	**2078 ± 12**	
	Zr D	1480	8	3530	0.136	0.12466 ± 213	2024 ± 30		
		1500	**66**	**14 500**	**0.146**	**0.12788 ± 63**	**2069 ± 9**		
		1520	**65**	**20 400**	**0.141**	**0.12805 ± 48**	**2071 ± 7**	**2070 ± 8**	
		1560	**7**	**5880**	**0.141**	**0.12847 ± 81**	**2077 ± 11**		
DL64	Zr B	**1500**	**46**	**1430**	**0.265**	**0.12825 ± 60**	**2074 ± 8**		**2074 ± 5**
		1520	**61**	**2770**	**0.247**	**0.12808 ± 50**	**2072 ± 7**		**MSWD = 0.58**
		1560	**62**	**3845**	**0.254**	**0.12795 ± 53**	**2070 ± 7**	**2072 ± 8**	**(10 steps)**
		1580	**8**	**4580**	**0.285**	**0.12837 ± 85**	**2076 ± 12**		
	Zr C	1500	26	1160	0.281	0.12672 ± 43	2053 ± 6		
		1520	**35**	**2715**	**0.203**	**0.12759 ± 61**	**2065 ± 8**	**2065 ± 8**	
	Zr D	**1480**	**15**	**2740**	**0.073**	**0.12885 ± 63**	**2082 ± 9**		
		1500	**45**	**2920**	**0.080**	**0.12896 ± 63**	**2084 ± 8**	**2083 ± 9**	

Table 1 *(Continued)*

Sample	Zircon	T (°C)	Number of ratios	$^{206}Pb/^{204}Pb$	$^{208}Pb/^{206}Pb$	$^{207}Pb^*/^{206}Pb^* \pm 1\sigma$	Step age $\pm 1\sigma$	Zircon age $\pm 1\sigma$	Mean age $\pm 2\sigma$
		1520	**8**	**6460**	**0.094**	**0.12874 ± 97**	**2081 ± 13**		
	Zr E	1480	22	1870	0.268	0.12679 ± 157	2054 ± 22		
		1500	**13**	**5340**	**0.231**	**0.12861 ± 67**	**2079 ± 9**	**2079 ± 9**	
	Zr F	**1480**	**51**	**7260**	**0.264**	**0.12775 ± 63**	**2067 ± 9**	**2067 ± 9**	
ID864	Zr A	1400	7	1930	0.114	0.12852 ± 286	2078 ± 39		2078 ± 7
		1420	**37**	**4780**	**0.115**	**0.12854 ± 78**	**2078 ± 11**		**MSWD = 0.04**
		1460	**72**	**7020**	**0.115**	**0.12846 ± 36**	**2077 ± 5**	**2077 ± 7**	**(8 steps)**
	Zr B	**1420**	**18**	**4450**	**0.104**	**0.12887 ± 105**	**2083 ± 14**		
		1460	**68**	**22 700**	**0.114**	**0.12848 ± 75**	**2077 ± 10**	**2078 ± 11**	
	Zr C	**1400**	**23**	**1550**	**0.084**	**0.12874 ± 128**	**2081 ± 17**		
		1420	**64**	**8210**	**0.086**	**0.12858 ± 88**	**2079 ± 12**		
		1460	**66**	**13 620**	**0.098**	**0.12854 ± 84**	**2078 ± 11**	**2079 ± 13**	
	Zr D	1420	7	9250	0.089	0.12827 ± 144	2074 ± 20		
	Zr E	1400	11	6410	0.104	0.12653 ± 122	2050 ± 17		
	Zr F	1400	7	4340	0.129	0.12615 ± 197	2045 ± 27		
		1460	**39**	**14 900**	**0.115**	**0.12838 ± 66**	**2076 ± 9**	**2076 ± 9**	

The errors on the ages per step and per zircon are given to 1σ (standard deviation). The mean age is the weighted mean of the different steps retained and is given to $\pm 2\sigma$ (95% confidence limit). The values in bold are those retained for the age calculation.
Pb* = radiogenic lead.

Table 2
Analytical data obtained through lead evaporation on single zircons at the Geochronological Laboratory of the Federal University of Para (Brazil)

Zircon	Temperature (°C)	Number of ratios	$^{206}Pb/^{204}Pb$	$^{208}Pb/^{206}Pb$	σ	$^{207}Pb/^{206}Pb$	σ	$^{207}Pb^{a}/^{206}Pb^{a}$	σ	Age (Ma) step	2σ	Age (Ma) grain	2σ
Clinopyroxene amphibole-bearing metagranite (Sample BEY1103)													
BEY1103/1	1500	90	32 258	0.17767	41	0.12971	18	0.12926	18	2088	3		
	1524	34	19 231	0.19983	271	0.13019	35	0.12939	37	2090	5	**2089**	**2**
BEY1103/2	1450	88	14 286	0.18262	52	0.13013	19	0.12925	19	2088	3		
	1500	84	31 250	0.20535	47	0.12955	20	0.12913	21	2086	3	**2087**	**2**
BEY1103/3	1450	54	23 256	0.14730	50	0.12978	45	0.12922	71	2088	10		
	1460	86	142 857	0.19423	317	0.12924	29	0.12914	27	2087	4		
	1480	88	166 667	0.21896	144	0.12923	19	0.12919	19	2087	3		
	1520	88	333 333	0.24825	183	0.12930	24	0.12926	24	2088	3	**2087**	**2**
BEY1103/4	*1450*	*16*	*3378*	*0.18140*	*108*	*0.13275*	*44*	*0.12885*	*58*	*2083*	*8*		
	1470	64	4184	0.18917	6l	0.13303	22	0.129850	25	2096	3	**2096**	**3**
BHY1103/5	1500	90	20 833	0.18784	340	0.12960	24	0.12897	28	2084	4		
	1550	88	37 037	0.23728	74	0.12947	19	0.12906	19	2086	3	**2085**	**2**
BEY1103/6	1450	88	12 821	0.16082	47	0.13024	19	0.12922	20	2088	3		
	1550	84	28 571	0.23880	82	0.12968	22	0.12922	23	2088	3	**2088**	**2**
BEY1103/7	1450	16	16 667	0.10689	83	0.13044	40	0.12965	41	2094	6		
	1500	84	22 727	0.18900	376	0.12971	17	0.12914	17	2087	2	**2088**	**5**
Mean (grains 1+2+3+5+6+7) 1062 ratios (USD = 1)												**2087**	**1**

Weighted mean and errors on the $^{207}Pb/^{206}Pb$ ages were calculated according to Gaudette et al. (1998). The values in bold are those retained for the age calculation. *Italic:* heating step not included in the calculation.
[a] Radiogenic lead.

The five zircons (A–E) analysed from granodiorite DL378 all provided a strong and stable Pb ion beam, defining a different number of steps depending on the zircon: one step for zircons A, B and E, four steps for zircon D, and six steps for zircon C (Table 1). Apart from zircon A, the ages obtained are coherent: 2080 ± 9 Ma for the six steps of zircon C and 2078 ± 8 Ma for the four steps of zircon D, and respectively 2076 ± 9 Ma and 2083 ± 8 Ma for the single steps of zircons B and E. A weighted mean age of 2081 ± 4 Ma was calculated using 12 steps (Fig. 5b), and corresponds to the age of crystallization of granodiorite DL378.

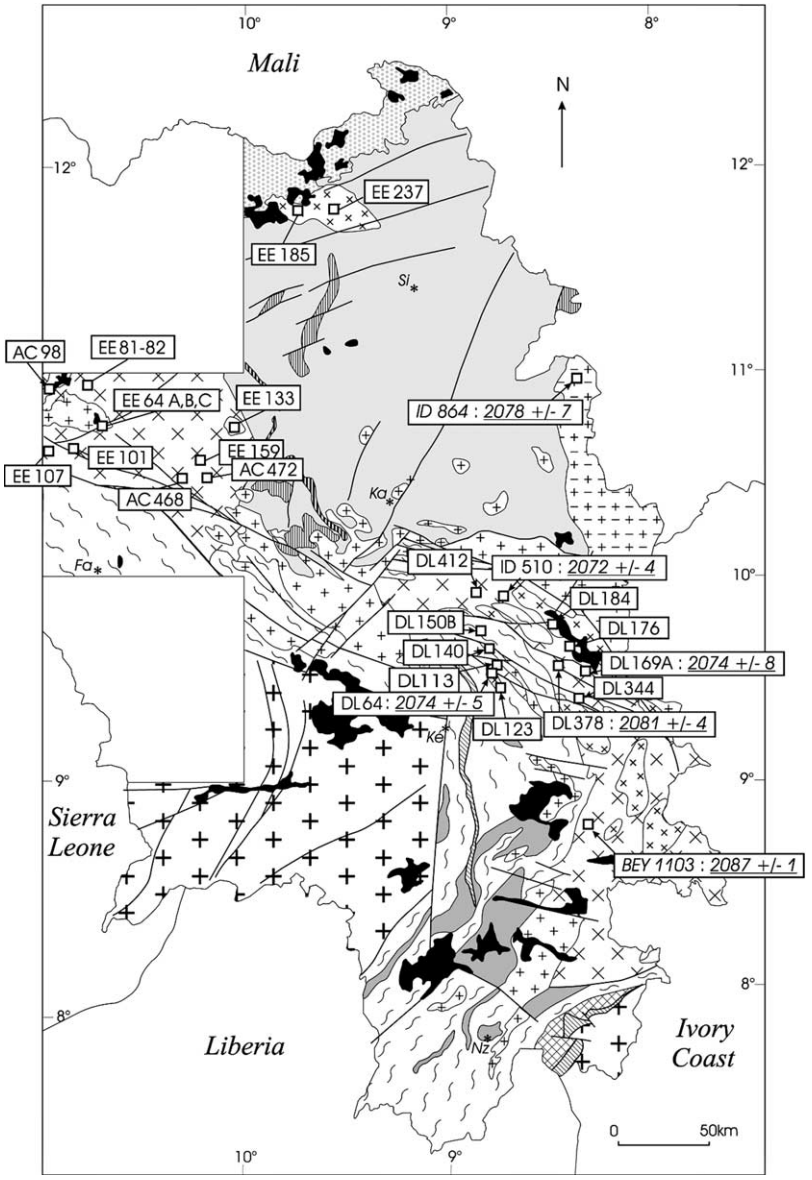

Fig. 4. Geological map showing the location of the analysed and/or dated samples, and the geochronological results. See Fig. 2 for lithological caption.

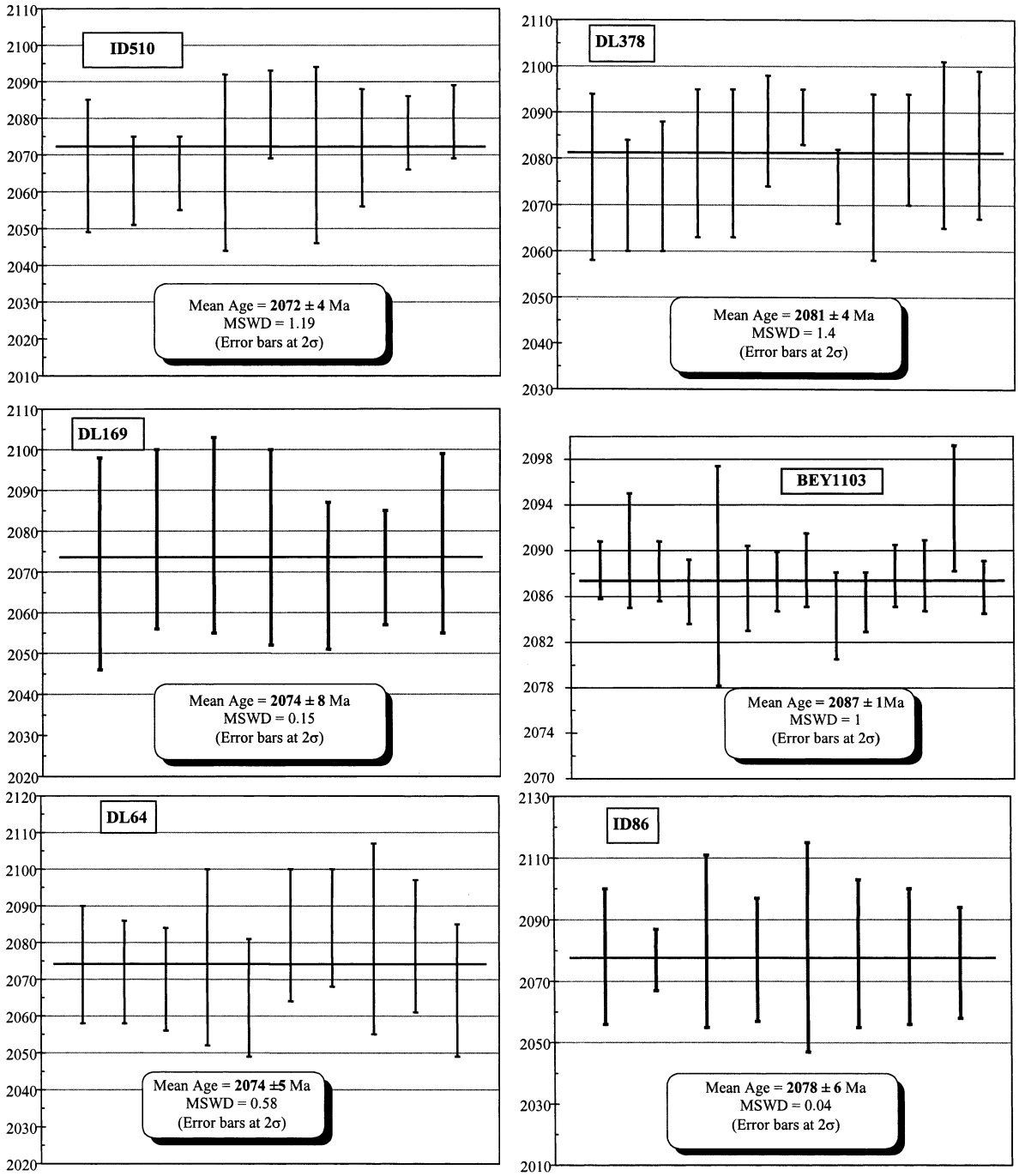

Fig. 5. Diagram of temperature step vs. $^{207}Pb/^{206}Pb$ age for the zircons of samples ID510 (a), DL378 (b), DL169 (c), BEY1103 (d), DL64 (e), and ID86 (f). The error bars on the ages per step are given to $\pm 1\sigma$ (standard deviation).

The four zircons selected from diorite DL169A were recorded on one to four temperature steps (Table 1). The first steps of zircons B and D yielded the youngest ages (<2070 Ma) and were discarded. The seven remaining steps yielded highly coherent ages, the weighted mean of which is 2074 ± 8 Ma (Fig. 5c), corresponding to the age of crystallization of diorite DL169A.

Seven zircons from the pyroxene-bearing granodiorite BEY1103 were analysed (Table 2) and, except for zircon no. 4, the isotopic results did not vary significantly between the different temperature steps and from one grain to another. The weighted mean age calculated on five grains is 2087 ± 1 Ma (2σ). Zircon no. 4 was not included in the age calculation because the high-temperature step yielded an age of 2096 Ma, which is older than the other dated zircons. The fact that no change was observed with increasing temperature during repeated analyses on a large number of crystals is a strong argument for retaining the age of 2087 ± 1 Ma (Fig. 5d) as the magmatic crystallization age of this metagranite. The age of 2096 ± 3 Ma yielded by zircon no. 4 suggests the existence of a lead-inherited component as old as 2096 Ma or more.

Overall, the ages obtained for the different types of the granodiorite suite seem perfectly coherent and indicate that the batholith was emplaced over a relatively short time interval, between 2090 and 2070 Ma.

4.2.2. Biotite granite

Dating attempts failed on the biotite granite from the northwestern part of the late Eburnean belt due to a lack of zircons of sufficient size and quality.

4.2.3. Monzogranite

A monzogranite sample (DL64) with microgranular texture was selected for geochronological analysis.

Of the seven zircons selected, five yielded stable Pb ion beam recorded over a total of 12 temperature steps (Table 1). Apart from the first step of zircons C and E, all the ages obtained are very similar, and are repeated over several steps for the single zircons B (2072 ± 8 Ma over four steps) and D (2083 ± 9 Ma over three steps). The weighted mean age calculated using the ten retained steps is 2074 ± 5 Ma (Fig. 5e) and corresponds to the age of crystallization of microgranite DL64, identical to the ages obtained for the granodiorite samples.

4.2.4. Two-mica granite

Six zircons from the two-mica granite (sample ID864) were selected and recorded over one to three temperature steps (Table 1). Zircon C yielded identical ages over three steps at 2080 Ma. This same age was obtained for the last two steps of zircon A, the two steps of zircon B, and the second step of zircon F. As the single steps of zircons D and E and the first steps of zircons A and F showed little resemblance, they were not retained for the age calculation. The weighted mean age calculated for eight temperature steps (Fig. 5f) is 2078 ± 7 Ma and is interpreted as the crystallization age of sample ID864. This age is similar to those obtained for the granodiorite and monzogranite.

5. Geochemistry of the plutonic belt

5.1. Analytical procedures

A total of 26 samples, spanning most of the plutonic rock types identified in the field, underwent geochemical analysis at BRGM, apart from the samples of two-mica granite, which were nonetheless dated. The location of the analysed samples is indicated on Fig. 4. The techniques used were X-ray fluorescence for major elements, and ICP–AES or ICP–MS for trace elements. In the range of contents corresponding to the studied rocks, the analytical uncertainties are generally $\leqslant 2\%$ for major elements and $\leqslant 10\%$ for trace elements, except for compatible elements (Mg, Co, Ni, Cr) whose contents in the most leucocratic rocks (biotite granite and monzogranite) are near the detection limit.

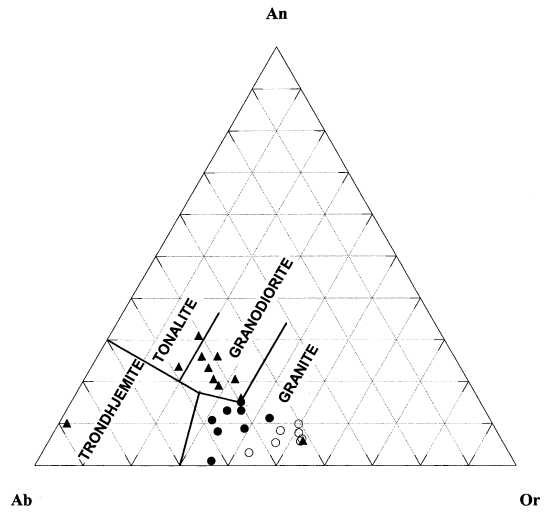

Fig. 6. Normative plots of Ab–Or–An (after O'Connor, 1965 and modified by Barker, 1979) for the granitic rocks of the late Eburnean plutonic belt of eastern Guinea. Solid triangle: granodiorite suite; empty circle: monzogranite suite; solid circle: biotite-granite suite (northwestern part of the belt).

5.2. Geochemical characterization

5.2.1. Granodiorite

Eleven samples were analysed (Table 3), including a syenite (DL344). The granodiorite shows an intermediate to slightly acid composition (SiO_2 = 54.6–68.8%), with most samples plotting in the granodiorite field on the Ab–Or–An diagram (Fig. 6), a position that reflects a relatively potassic nature. One sample, corresponding to an albitized rock (DL176, $Na_2O = 7.6\%$; $K_2O = 0.2\%$), plots in the trondhjemite field, whereas another sample of a syenitic nature (DL344, $Na_2O = 4.2\%$; $K_2O = 7.58\%$), is defined as a granite$_{sl}$ (quartz-bearing syenite). All the rocks are metaluminous (A/CNK index from 0.68 to 0.94) (Table 3) and present a low to moderate FeO_t/MgO ratio (1.5–3) (Fig. 7). These trends point towards a calc-alkaline nature, but the absence of a correlation between FeO_t/MgO and SiO_2 (Fig. 7) indicates that the granodiorite does not constitute a single differentiation suite.

The primordial mantle-normalized incompatible element patterns (Fig. 8) show the homogeneity of the 'geochemical signatures' of the granodiorite and the specific characteristics of the albitized rock (DL176). The granodiorite provides patterns that are fairly fractionated with constant negative anomalies in U, Ta, Nb, P and Ti, and

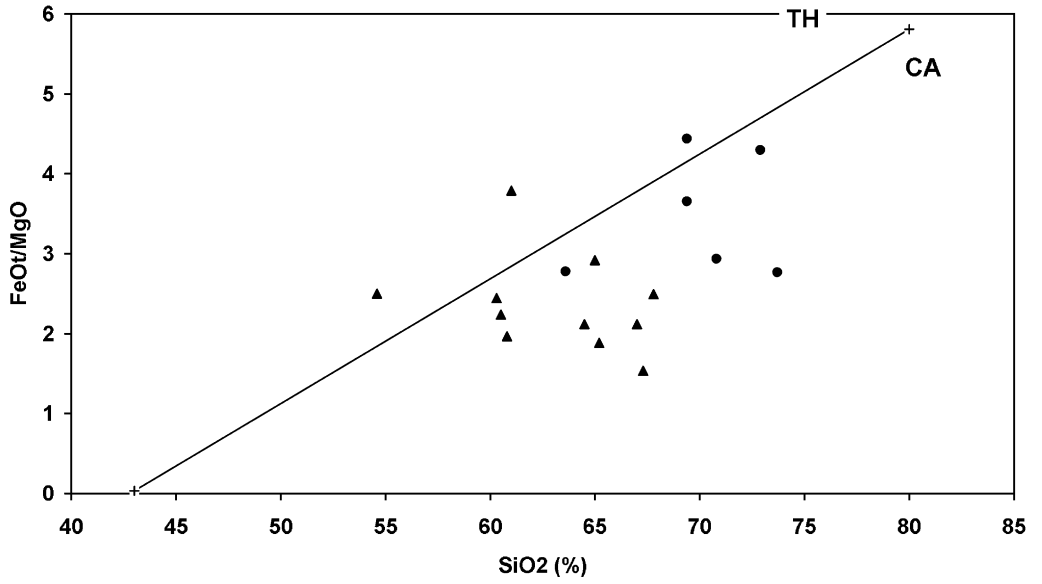

Fig. 7. SiO_2 vs. FeO_t/MgO diagram (Miyashiro, 1974) for the granodiorite and biotite-granite suites of the late Eburnean plutonic belt of eastern Guinea. Symbols as in Fig. 6. TH, field of the tholeiitic series, CA, field of the calc-alkaline series.

Table 3
Chemical analyses for the granodiorite suite (including the syenite DL344)

	Granodiorites											Syenite	Central Andes average		
Age in Ma	2074 ± 8	2081 ± 4							2072 ± 4				Calc-alkaline lavas. SiO_2 = 60–68%		
Sample	DL169A	DL378	DL176	DL113	AC468	DL140	EE107	EE159	ID510	EE101	Average	DL344	Average	Standard deviation	*n*
SiO_2 (%)	54.6	60.3	60.5	60.8	64.5	65	65.2	67	67.3	67.8	63.3	61.0	63.2	1.78	418
TiO_2	1.73	0.46	0.63	0.63	0.58	0.47	0.57	0.51	0.58	0.39	0.66	0.71	0.8	0.17	382
Al_2O_3	14.4	18.9	15.4	15.9	16.4	16.1	15.1	15.2	15.3	15	15.8	17.0	16.27	0.73	383
Fe_2O_{3t}	11.65	4.07	6.72	6.33	4.24	5.19	4.6	3.77	3.93	3.6	5.41	5.05	4.96	1.09	391
MnO	0.15	0.09	0.13	0.13	0.07	0.1	0.07	0.06	0.08	0.09	0.1	0.1	0.08	0.04	383
MgO	4.2	1.5	2.7	2.9	1.8	1.6	2.2	1.6	2.3	1.3	2.2	1.2	2.14	0.61	383
CaO	6.6	4.9	5.4	4.9	3.6	3.8	3.5	2.9	4.2	2.6	4.2	2.2	4.53	2.35	383
Na_2O	3.5	5.6	7.6	3.9	4.5	4.3	3.8	4.2	4	4	4.5	4.2	3.78	0.57	383
K_2O	1.82	2.46	0.2	2.81	3.26	2.85	3.51	3.27	2.35	4.02	2.66	7.58	3.11	0.53	413
P_2O_5	0.44	0.31	0.18	0.22	0.25	0.21	0.24	0.24	0.15	0.18	0.24	0.36	0.39	0.08	326
LOI	0.4	0.6	0.5	0.6	0.3	0.3	0.5	0.4	0.4	0.4	0.4	0.3	1.17	–	–
Sum	99.49	99.19	99.96	99.12	99.5	99.92	99.29	99.15	100.59	99.38		99.7			
Li(ppm)	14	14	<1	21	15	21	11	15	18	16	16	8	17	6	71
Rb	96	57	9	91	87	114	125	91	138	109	92	180	109	42	377
Ba	1206	653	533	1316	2182	938	1294	1852	323	1751	1205	1220	869	289	322
Sr	617	680	1079	655	938	534	507	847	339	830	703	702	558	180	399
U	0.9	2.4	3.9	0.9	1.6	1.2	0.7	1.3	1.6	0.9	1.5	5.7	4.16	2.9	143
Th	7.0	49.6	12.4	11.1	11.3	11.5	24.5	8.9	26.2	17.6	18.0	43.1	13.9	7.4	176
Ta	1.4	1	1.2	0.4	1.7	0.6	1.3	0.7	1	1.7	1.1	4.9	1.27	0.73	127
Nb	17.6	10.4	17.0	9.0	15.2	11.9	16.4	9.4	19.6	13.9	14.0	58.6	12.8	6.4	167
Hf	7.2	10.3	6.3	7	5.1	5.7	7.8	5.6	4.4	3.7	6.3	16.2	5.41	0.65	148
Zr	206	284	189	218	185	184	238	186	123	122	194	647	195	35	241
Y	18.0	14.8	19.5	12.3	16.6	22.6	16.6	8.2	13.4	10.9	15.3	37.6	17.5	5.4	160
Ni	54	16	27	26	30	12	37	29	35	15	28	6	16	11	290
Cr	86	44	167	120	33	78	51	25	55	71	73	15	37	31	262
Co	35	8	16	19	10	13	10	9	13	9	14	7	18	9	261
V	166	56	143	120	70	58	72	59	54	48	85	53	107	30	225
La	43.5	57.2	52.2	46.3	55.3	38.9	59.8	42.0	29.7	41.9	46.7	108.8	39.0	9.7	184
Ce	89.0	103.5	101.2	83.7	110.7	80.6	120.6	86.6	59.6	80.8	91.6	256.2	80.0	22.1	149
Pr	10.4	11.0	11.0	7.9	12.3	9.4	12.8	9.5	6.7	8.4	9.9	30.0	–	–	–
Nd	42.6	40.2	42.0	27.6	45.1	36.3	48.0	33.8	25.5	29.4	37.1	110.8	35.0	9.8	103
Sm	7.9	6.7	6.7	4.7	6.9	7.9	7.9	5.0	5.1	3.8	6.3	18.4	6.4	1.5	120
Eu	2.1	1.0	1.4	1.2	1.6	1.4	1.3	1.3	1.0	1.1	1.3	3.2	1.4	0.31	189
Gd	6.0	4.5	5.6	3.8	6.0	6.8	5.8	4.1	3.8	3.0	4.9	12.0	5.03	1.4	24
Tb	0.8	0.6	0.8	0.5	0.7	0.9	0.7	0.5	0.5	0.4	0.6	1.6	0.6	0.14	179
Dy	4.0	3.3	3.8	2.6	3.2	4.6	3.4	1.9	2.8	2.0	3.2	8.2	3.0	0.73	11
Ho	0.8	0.5	0.7	0.5	0.5	0.9	0.5	0.3	0.5	0.3	0.5	1.4	–	–	–
Er	2.1	1.4	2.1	1.4	1.2	2.4	1.2	0.7	1.4	0.8	1.5	3.8	1.2	0.32	10
Tm	0.3	0.2	0.3	0.2	0.2	0.3	0.2	0.1	02	0.1	0.2	0.5	–	–	–
Yb	1.7	1.2	1.9	1.1	1.2	1.8	0.9	0.6	1.2	0.7	1.2	3.4	1.4	0.54	130
Lu	0.3	0.2	0.3	0.2	0.2	0.2	0.1	0.1	0.2	0.1	0.2	0.5	0.2	0.07	115
A/CNK	0.72	0.89	0.68	0.85	0.92	0.92	0.89	0.94	0.9	0.93	0.86	0.84	0.89		

A/CNK is the aluminous index, $Al_2O_3/CaO+Na_2O+K_2O$ in atomic proportions. The average composition (and standard deviation) of the high-K calc-alkaline andesite and dacite from the central Andes is given for comparison (BRGM geochemical database on Andean magmatic rocks (Thiéblemont, 1999)) and was calculated using a number of measurements that varied depending on the element.

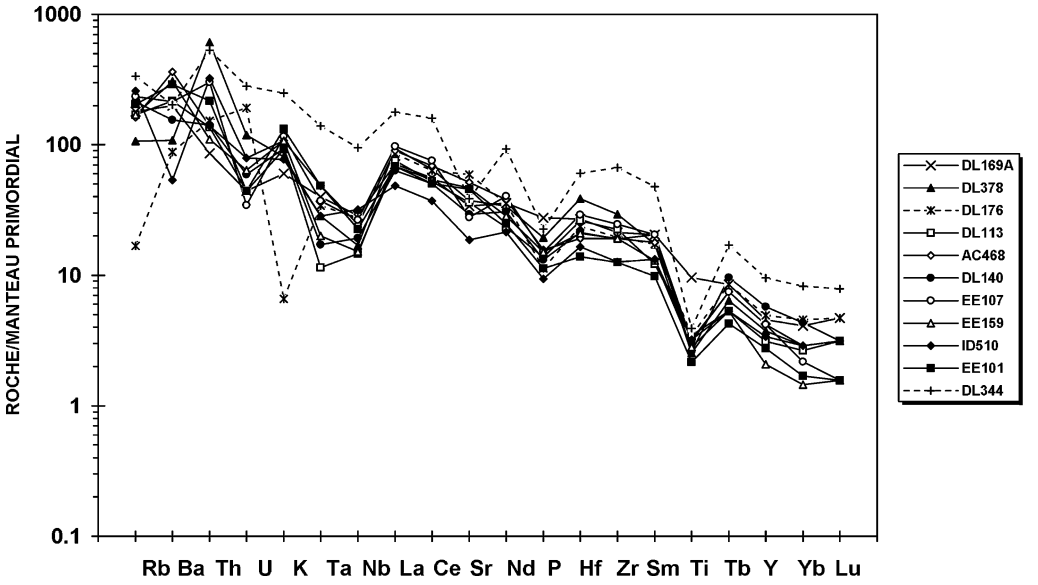

Fig. 8. Primordial mantle-normalized (normalization values from Hofmann, 1988) incompatible element patterns for the granodiorite suite. Sample DL344 is a quartz syenite from this suite.

'accidental' positive anomalies in Th (samples DL378, EE107, ID510). These spectra are comparable to those of present-day calc-alkaline rocks (Briqueu et al., 1984). The albitized sample is marked by negative anomalies in Rb and K attributed to weathering.

The Zr vs. $(Nb/Zr)_N$ diagram (Fig. 9) was used to clarify the granodiorite signatures and made it possible to discriminate two types of recent calc-alkaline rocks, namely an essentially 'mantle' type confined to subduction zones, and a more ubiquitous 'crustal' type (Thiéblemont, 1999). The granodiorite plots within the field of crustal-contaminated calc-alkaline rocks, which is consistent with the high contents of K, Th and light rare earths (e.g. $K_2O = 1.82–4.02\%$; Th = 7–49.6 ppm; La = 29.7–59.8 ppm), incompatible elements that are concentrated in the continental crust.

Finally, the syenite (DL344) is clearly distinct from the granodiorite, showing higher contents in almost all incompatible elements and weak negative anomalies in Ta and Nb.

5.2.2. Biotite granite

Eight analyses were carried out on the biotite granite sampled from different plutons in the northwestern part of the late Eburnean belt (Table 4). The rocks are slightly to highly acid ($SiO_2 = 63.6–76.1\%$), rich in potassium ($K_2O = 3.4–5.24$), and metaluminous to slightly peraluminous (A/CNK = 0.94–1.01). They plot in the granite field on the Ab–Or–An diagram (Fig. 6). The moderate FeO_t/MgO ratios (Fig. 7) and relatively high Al_2O_3 contents (13.8–16.5%) characterize the rocks as calc-alkaline.

Despite the marked variation in incompatible element contents revealed by the incompatible element patterns (Fig. 10A), most of the granites analysed showed common features and, more specifically, strong negative anomalies in Ta and Nb, variable negatives anomalies in Sr, P and Ti, and a fairly marked fractionation between heavy rare earths. Two rocks nevertheless stand out: the granite EE64C, which is highly leucocratic ($SiO_2 = 76.1\%$; $Fe_2O_{3t} = 0.64\%$) and depleted in Ba, Sr, Th, Zr and light rare earths, and the

Table 4
Chemical analyses for the biotite-granite suite and comparison with the average composition of late Miocene to Recent rhyodacite and rhyolite from the central Andes

Sample	Biotite granites									Central Andes average		
	EE081	EE064A	EE064B	EE082	AC098	AC472	EE133	EE064C	Average	calc-alkaline lavas. SiO2 = 88–72%		
										Average	Standard deviation	*n*
SiO_2 (%)	63.6	69.4	69.4	70.8	71.8	72.9	73.7	76.1	69.7	89.5	1.2	78
TiO_2	0.64	0.31	0.37	0.33	0.07	0.23	0.09	<0.05	0.33	0.48	0.16	75
Al_2O_3	16.5	15.3	15.3	14.8	15.4	14.6	13.8	13.8	15.3	15.07	0.78	75
Fe_2O_{3t}	4.32	2.84	2.96	2.61	1.81	1.91	1.23	0.64	2.74	2.78	0.97	78
MnO	0.05	0.07	0.06	0.07	0.03	0.06	0.06	<0.02	0.06	0.06	0.08	74
MgO	1.4	0.7	0.6	0.8	<0.2	0.4	0.4	<0.2	0.7	0.98	0.42	76
CaO	2.7	2	1.8	2.1	0.3	1.3	1.4	1.1	1.7	2.8	0.72	76
Na_2O	4.4	4.2	3.9	4.4	5.6	4.2	4.4	4.6	4.5	3.45	0.7	78
K_2O	4.45	4.29	5.24	3.9	4.58	4.49	3.4	3.83	4.49	4.00	0.9	78
P_2O_5	0.36	0.13	0.14	0.14	0.11	0.08	<0.05	<0.05	0.16	0.14	0.06	72
LOI	0.6	0.4	0.7	0.3	0.5	0.5	0.6	0.2	0.5			
Sum	99.02	99.64	100.47	100.25	100.2	100.67	99.08	100.27				
Li (%)	15	25	25	17	5	12	27	4	17			
Rb	165	161	174	114	189	171	109	157	162	186	69	65
Ba	1888	1999	2280	1084	1120	1148	793	106	1587	665	259	61
Sr	582	641	468	543	86	311	242	95	439	360	145	66
U	5.4	3	2	1.5	5.1	4.8	2.7	9.4	3.6	6.4	4.4	23
Th	28.1	21.2	23.9	10.6	17.8	29.4	8.2	7.9	21.8	19.9	8.4	50
Ta	2.1	1.1	1.6	0.9	0.5	1.5	1.2	1.2	1.3	1.4	1.00	21
Nb	29.4	14.2	19.9	11.7	9.9	13.8	10.2	7.7	16.5	16.0	5.9	34
Hf	11.5	6	8.9	4.4	11.7	5.8	2.9	1	8.1	4.3	0.44	22
Zr	412	209	317	141		170	77	20	250	155	38	48
Y	14.4	8.8	15.8	8.3	4.9	9.8	7.3	7.7	10.3	14.5	6.4	42
Ni	11	14	14	15	4	10	5	5	11	11	13	52
Cr	24	34	41	39	11	45	46	13	32	22	14	44
Co	10	4	5	5	1	3	2	<1	4	7	9	25
V	64	29	34	30	8	17	10	3	30	39	17	25
La	121.7	71.0	110.5	36.1	41.1	51.3	21.9	7.4	72	35.0	14.0	26
Ce	235.9	126.8	209.1	71.0	69.4	91.3	40.0	9.9	133.9	65.3	23.7	40
Pr	22.4	12.3	19.9	7.7	6.8	8.6	3.8	1.1	13			
Nd	72.8	39.8	63.3	27.7	20.1	28.7	13.5	4.3	42.1	28.3	11.3	23
Sm	9.6	4.9	8.3	4.8	2.4	3.8	2.0	0.8	5.6	5.0	2.0	23
Eu	1.9	1.1	1.6	1.0	0.4	0.8	0.5	0.3	1.13	1.00	0.31	24
Gd	4.2	4.6	7.0	3.8	2.0	3.3	1.1	1.0	4.2			
Tb	0.5	0.5	0.9	0.4	0.3	0.4	0.2	0.2	0.5	0.42	0.22	19
Dy	2.6	2.0	3.7	1.8	1.1	1.9	0.9	1.3	2.2			
Ho	0.4	0.3	0.6	0.3	0.2	0.3	0.2	0.2	0.4			
Er	1.3	0.8	1.6	0.8	0.4	0.8	0.7	0.7	1			
Tm	0.2	0.1	0.2	0.1	0.1	0.1	0.1	0.1	0.1			
Yb	1.0	0.6	1.3	0.7	0.3	0.7	0.8	0.7	0.8	1.1	0.7	23
Lu	0.1	0.1	0.2	0.1	0.1	0.1	0.1	0.1	0.12	0.18	0.12	13
A/CNK	0.94	0.97	0.95	0.94	1.01	0.99	0.99	0.97	0.97			

granite EE133, which is poor in Th, and whose pattern shows no fractionation between heavy rare earths. Sample EE64C presents features characteristic of many leucogranites, commonly attributed to fractionation of monazite (Th, light rare earths), zircon (Hf, Zr) and feldspar (Sr, Ba), and reflecting a low temperature of acid magma (Mittlefehldt and Miller, 1983). These features are less marked in sample EE133, which is particularly depleted in all heavy rare earths (e.g. Gd = 1.1 ppm).

The different types of 'common' biotite granite (excluding the previous two rocks) were compared by redrawing the patterns after normalization of the compositions to a common La value. The analogies are thus highlighted (Fig. 10B), the patterns being also fairly similar to those of the granodiorite (Fig. 8). Finally, the analytical results were recorded on the Zr vs. $(Nb/Zr)_N$ diagram (Fig. 9); most biotite granite samples plot in the immediate vicinity of the granodiorite, i.e. in the 'crustal' calc-alkaline magmatic field (Thiéblemont, 1999). The two most acid granites (EE133 and EE64C) plot away from the others in the field of the peraluminous leucogranite (Fig. 9).

5.2.3. Monzogranite

The monzogranite (seven samples analysed, Table 5) has an acid (SiO_2 = 72.4–75.58%), highly potassic (K_2O = 4.64–5.74%), and metaluminous to slightly peraluminous (A/CNK = 0.94–1.01) (Table 5) composition. It plots in the granite field on the Ab–Or–An diagram (Fig. 6). Th contents can be very high (> 50 ppm), whereas Al_2O_3 (12.5–14%) and Sr (20–231 ppm) contents are low to moderate.

The primordial mantle-normalized incompatible element patterns (Fig. 11) show strong analogies between the different rocks: marked enrichment in Rb, Th and light rare earths, strong negative anomalies in Ta and Nb, weak negative anomalies in Ba, Sr, P and Ti suggesting a limited fractionation of alkaline feldspar (Ba), plagioclase (Sr), apatite (P) and ferro-titaniferous oxides (Ti). These analogies aside, however, a marked variability in contents is observed, which is maximal for Ta and Nb (respectively 0.2–1.6 ppm and 2–20.4 ppm), high for Th and rare earths (Th = 19.6–70.5; La = 30.8–110.2 ppm; Yb = 0.3–1.2 ppm), and low for Rb, Hf and Zr (Rb = 191–290 ppm; Zr = 94–184 ppm). This variability is reflected by the Zr vs. $(Nb/Zr)_N$ diagram (Fig. 9),

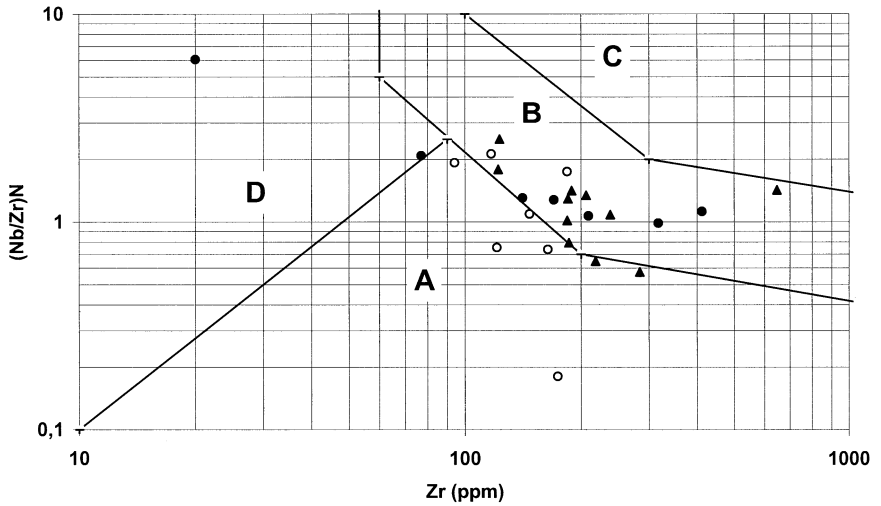

Fig. 9. Zr vs. $(Nb/Zr)_N$ diagram (Thiéblemont and Tegyey, 1994; Thiéblemont, 1999) for the granitic rocks of the late Eburnean plutonic belt of eastern Guinea. Symbols as in Fig. 6. (A) field of recent mantle-derived subduction-zone magmatic rocks; (B) field of crustal-contaminated calc-alkaline rocks; (C) field of intra-plate magmatism; (D) field of peraluminous leucogranite.

Table 5
Chemical analyses for the monzogranite suite and comparison with the average composition of late Miocene to Recent rhyolite from the central Andes

	Monzogranites								Central Andes average		
Age in Ma	2074 ± 5								Calc-alkaline lavas. SiO2 > 70%		
Sample	DL184	DL123	EE185	DL412	DL64	EE237	DL150B	Average	Average	Standard deviation	*n*
SiO_2 (%)	72.4	73.7	73.2	75.5	74.1	74	75	74	72.74	2.16	89
TiO_2	0.17	0.16	0.23	0.09	0.2	0.15	0.13	0.16	0.26	0.14	83
Al_2O_3	13.8	13.7	14	12.5	13.8	13.5	13.6	13.6	14.13	1.25	83
Fe_2O_{3t}	1.9	1.67	1.9	1.43	1.88	1.29	1.45	1.65	1.66	0.8	83
MnO	0.05	0.04	0.04	0.05	0.03	0.04	0.04	0.04	0.06	0.03	82
MgO	0.3	<0.2	0.5	<0.2	<0.2	0.4	<0.2	<0.5	0.49	0.32	84
CaO	1.4	0.8	1.1	0.5	0.9	0.7	1.1	0.9	1.58	0.81	84
Na_2O	3.2	3.2	3.2	4.1	3.2	3.6	3.5	3.4	3.66	0.79	84
K_2O	5.62	5.66	5.6	4.64	5.74	5.12	5.2	5.37	4.31	0.97	89
P_2O_5	0.06	0.05	0.07	<0.05	0.06	<0.05	<0.05	−0.05	0.08	0.06	75
LOI	0.3	0.3	0.4	0.3	0.3	0.5	0.3	0.34			
Sum	99.2	99.28	100.24	99.11	100.21	99.3	100.32				
Li (ppm)	20	18	32	8	30	48	4	23			
Rb	201	191	206	193	275	290	176	219	177	95	71
Ba	1087	911	907	206	1486	612	663	839	626	350	56
Sr	231	108	221	20	114	128	167	141	260	190	71
U	6.8	2.5	4.1	3.4	3.4	3.9	4.4	4.1	7.3	5.33	30
Th	60.0	45.2	19.6	22.6	70.5	20.2	25.2	37.6	18.3	10.5	38
Ta	0.2	0.4	0.5	0.3	1.1	1.2	1.6	0.8	1.67	1.55	30
Nb	2.0	5.8	7.7	102	20.4	11.5	15.8	10.5	18.4	7.9	24
Hf	6.2	4.4	6.4	5.9	6	4.1	4.8	5.4	4.07	0.84	30
Zr	174	121	164	147	184	94	117	143	158	68.4	49
Y	2.3	5.2	17.9	13.5	12.4	12.2	10.7	10.6	16.4	10.3	35
Ni	4	3	4	2	2	3	4	3	9	21	47
Cr	63	47	25	22	16	22	51	35	10	9	38
Co	3	2	2	<1	1	2	3	2	9	14.4	42
V	17	10	25	3	8	15	13	13	23	18.4	27
La	66.8	58.7	59.4	30.8	110.2	44.8	37.4	58.3	28.2	10.1	35
Ce	114.1	105.3	107.2	59.8	212.1	84.9	65.5	107.4	53.3	17.9	36
Pr	9.8	9.9	9.8	6.3	19.5	7.7	6.0	9.9			
Nd	27.0	30.0	27.3	22.9	62.1	22.6	21.0	30.4	21.8	8.9	29
Sm	3.0	3.4	3.8	5.0	9.1	3.1	3.0	4.3	4.5	1.4	28
Eu	0.7	0.6	0.5	0.2	0.8	0.4	0.5	0.53	0.85	0.49	35
Gd	2.3	3.0	3.0	3.4	6.5	2.6	2.4	3.3			
Tb	0.2	0.3	0.4	0.5	0.8	0.4	0.3	0.4	0.4	0.15	32
Dy	0.6	1.3	1.8	2.8	3.2	1.9	1.9	1.9			
Ho	0.1	0.2	0.3	0.6	0.5	0.4	0.3	0.3			
Er	0.3	0.5	1.0	1.4	1.3	1.0	0.9	0.9			
Tm	0.1	0.1	0.2	0.2	0.2	0.2	0.1	0.2			
Yb	0.3	0.5	1.0	1.2	1.1	1.2	0.7	0.9	1.3	0.78	28
Lu	0.1	0.1	0.2	0.2	0.2	0.2	0.1	0.16	0.2	0.15	15
A/CNK	0.94	1.01	1.00	0.94	0.99	1.01	0.97	0.98	1.00		

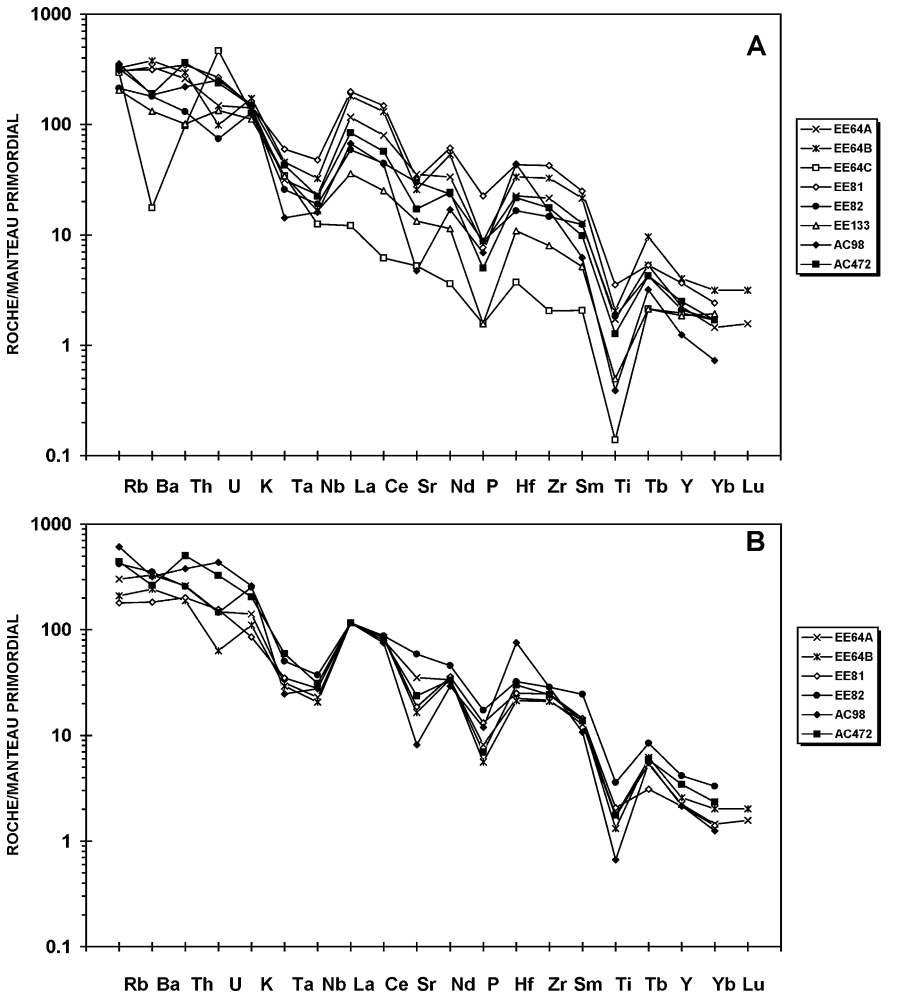

Fig. 10. (A) Primordial mantle-normalized (normalization values from Hofmann, 1988) incompatible element patterns for the biotite-granite suite of the northwestern part of the belt. (B) Primordial mantle-normalized incompatible element patterns for six samples of the biotite-granite suite, normalized to a constant $(La)_N$ value. The normalization procedure emphasises the similarities between the different samples irrespective of the absolute abundance of incompatible elements.

where the monzogranite samples are scattered between two fields, one corresponding to 'crustal-contaminated' subduction- or collision-related calc-alkaline rocks, and the other to mainly 'mantle-derived' subduction-related rocks. The previous trends are independent of silica content, which suggests that the monzogranite does not constitute a homogeneous petrological group. This may reflect a heterogeneity in the source material and/or melting conditions (pressure, temperature, etc).

5.2.4. Two-mica granite

Although no geochemical analysis was carried out on the two-mica granite, its mineral composition is nevertheless of a clearly acid and strongly peraluminous nature.

6. Structure of the plutonic belt

The structure of the plutonic belt in eastern Guinea is essentially characterized by the general

geometry of this belt (plutons and their internal fabric) oriented around the Archean Kénéma–Man core, and by the presence of major WNW–ESE to NW–SE-trending sinistral strike–slip faults affecting the central and northern parts of the belt.

6.1. Geometry of the plutonic belt rocks and syn-magmatic fabric

Apart from the two-mica granite and some small intrusions within the Siguiri Basin, the granitic rocks constitute a belt parallel to the margin of the Archean core (Fig. 2 and Fig. 3): WNW–ESE in the northwest, W–E along the southern edge of the Siguiri Basin, and then NW–SE and NNE–SSW towards the south. Within the belt, the individual plutons show a varying degree of anisotropy in accordance with the overall direction of the belt. Finally, within the actual plutons (except the two-mica granite), and at some distance from the intense deformation zones (described in the next paragraph), a subvertical and generally weak magmatic fabric is observed locally, as well as magmatic layering particularly marked by elongated and aligned enclaves. The orientation of these syn-magmatic anisotropies also seems consistent with the general orientation of the belt. These observations suggest that the plutonic belt was emplaced and crystallized under a stress regime and that it was moulded in a subsolidus state around the edge of the Kénéma–Man craton.

6.2. Major regional structures: WNW–ESE-trending sinistral strike–slip faults

The central part of the plutonic belt is extensively affected by major sinistral ductile strike–slip faults generally trending WNW–ESE (locally W–E or NW–SE) (Fig. 3). These faults are observed at several outcrops where they show a thickness of deca-hectometre scale and a commonly intense mylonitic to ultramylonitic deformation. They are generally easily identified on aeromagnetic maps, occurring in close succession over large distances and constituting a variably anastomosing network.

The sinistral kinematics of these faults have been well characterized at numerous outcrops based on various criteria depending on the rock type and location: asymmetric quartz crystallization in pressure shadow zones of feldspar phenocrysts, C/S or

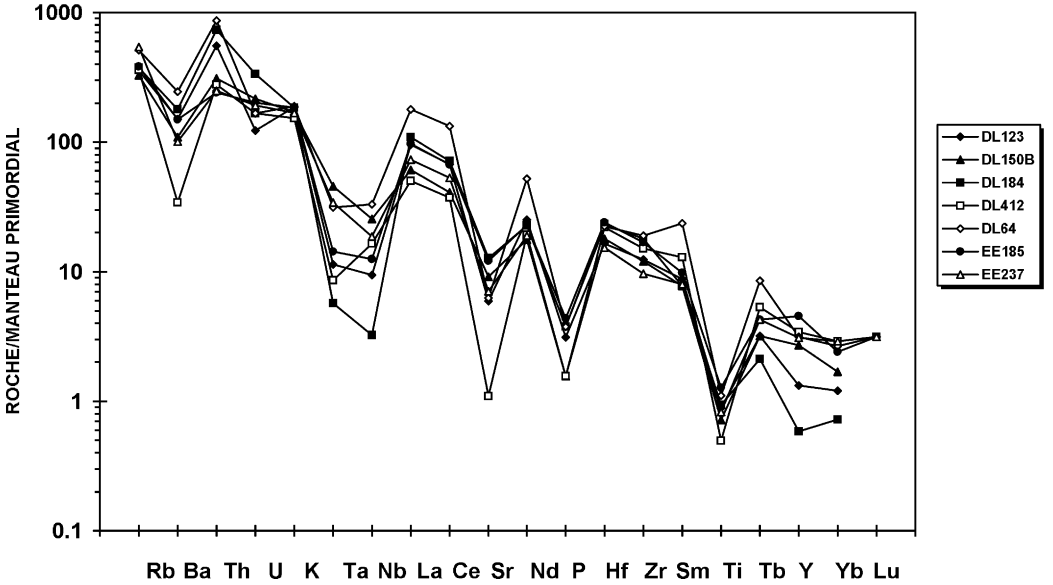

Fig. 11. Primordial mantle-normalized (normalization values from Hofmann, 1988) incompatible element patterns for certain granites of the monzogranite suite.

C′/S relationships, mica 'fish' (in the mica schist along the edge of the Siguiri Basin).

In the south of the Siguiri Basin, the continuation of strike–slip shear zones takes the form of local thrust planes showing southward or, more rarely, northward vergence. Feybesse et al. (1999) consider this thrusting to be associated with early regional thickening prior to sinistral tectonism. However, as these thrusts have a limited geographic extent and show a global orientation similar to the adjacent strike–slip shear zones of which they are the continuation, the hypothesis that they are in fact local thrusts associated in a transpressive context with the regional strike–slip tectonism can be put forward.

In general, the mylonitic deformation in the strike–slip zones is mainly accommodated by quartz (bands, intense recrystallization, crystallization in pressure shadows, etc.), whereas feldspar crystals persist as clasts that are fractured to varying degrees (rounded in the ultramylonitic zones). The temperature conditions were thus relatively low (300–400 °C) during mylonitization, as confirmed by the crystallization of phyllitic minerals of relatively low temperature and the absence of recrystallized amphibole in the shear zones. Nonetheless, the syn-magmatic fabric of the granitic rocks locally highlights 'warmer' shear zones under 'subsolidus' conditions (with the injection of pegmatite dykes) showing geometries and kinematics that are consistent with those of the 'colder' mylonitic zones. This suggests the onset of major strike–slip tectonism under subsolidus conditions before crystallization of the plutons had totally finished.

Strike–slip deformation does not affect all the granitic rock types of the belt. It is particularly well marked in the granodiorite, whereas the monzogranite locally cuts the shear zones; this indicates that the shear zones were formed before intrusion of the monzogranite, but after crystallization of the granodiorite. The shear zones thus appear globally contemporaneous with plutonic belt emplacement at about 2075 Ma.

The shear zones are mainly located within the plutonic belt, particularly within a restricted zone along the northwestern margin of the Archean domain, which presents a similar orientation to the shear zones. Evidence of strike–slip tectonism is absent within the northern extensions of the plutonic belt and throughout most of the Siguiri Basin, but observed along its southern edge. In addition, syn-schistose deformation identified within the basin does not appear to be clearly linked to the strike–slip tectonism.

Similarly, WNW–ESE-trending strike–slip faults have nowhere been observed along the south-eastern edge of the plutonic belt in the Guinean forest region (Fig. 3), and the global orientation of the foliation in both Archean and Paleoproterozoic rocks is almost orthogonal (NNE–SSW) to that of the strike–slip faults, suggesting the absence of WNW–ESE-trending sinistral kinematics in this area.

Several of these shear zones extend over limited distances within the Archean. Some are located along the contact between the plutonic belt and the Archean; this is especially the case in the western part of the study area where a major strike–slip zone marks the boundary between the Kénéma–Man craton and the plutonic belt.

7. Discussion

7.1. Late Eburnean age of the plutonic belt

Geochronological datings were carried out for most of the rock types (except for the biotite granite) and suggest an emplacement over a short interval of time for all the plutonic rocks. The granodiorite was intruded between c. 2090 and 2070 Ma and, despite local evidence indicating its posteriority (veins, granodiorite enclaves), the monzogranite yields a similar geochronological age (2074 Ma). Along the eastern edge of the Siguiri Basin, the two-mica granite was also intruded within the same time interval of 2090–2070 Ma (2078 Ma).

This time interval of 2090–2070 Ma corresponds to a late period within the context of Eburnean evolution of the Paleoproterozoic Baoulé-Mossi domain of West Africa: all the granitic rocks previously dated in this domain outside of Guinea, mainly in Ghana and the Ivory Coast, yielded ages between 2180 Ma and 2085 Ma, with two main groups of ages around 2175 and 2100 Ma (Hirdes

et al., 1992, 1996; Oberthür et al., 1998). We thus attribute a 'late Eburnean' character to the plutonic belt of eastern Guinea.

It should be noted that Eburnean migmatite and granite also exist to the south of 8°N. These rocks are more recent (c. 2050–2020 Ma; Thiéblemont et al., 1999) than the granitic rocks of the plutonic belt and are attributed to a distinct geodynamic event (Delor et al., personal communication).

Before the period 2090–2070 Ma, all the ages obtained for the gneiss and granitic rocks of eastern Guinea fall clearly within the Archean (Bering et al., 1998; Thiéblemont et al., 2001), with the most recent reflecting the importance of Liberian events (c. 2700–2800 Ma) in the formation of this craton. It thus seems that the margin of the Archean craton remained 'inert' and stable during most of the Birimian cycle (c. 2200–2090 Ma), and only became active during a late stage of the cycle (late Eburnean). Furthermore, the small range of ages points towards the late Eburnean granitization (and deformation) being attributed to a single cause, which we shall try to constrain further on the basis of the geochemical and structural data.

7.2. An active-margin-related magmatism?

The granitic rocks of the late Eburnean belt show strong chemical analogies (calc-alkaline nature, high Th/Ta and La/Nb ratios, etc.) with the magmatic suites of recent active margins (e.g. Gill, 1981). These granitic rocks are also marked by high K_2O contents and an essentially intermediate to acid composition, characteristics that are frequently associated with a major crustal participation in magma generation. Such 'contamination' is well documented for the recent volcanic suites of the central Andes where it is attributed to the intense thickening of this margin (e.g. Hildreth and Moorbath, 1988). A BRGM database, including a compilation of analyses of recent Andean lavas, was used to test further this analogy between the late Eburnean belt and Andean magmatism. For each family of granitic rocks, a 'set' of analyses on Andean lavas showing the same range of SiO_2 contents was extracted and averages were calculated (Tables 3–5). Only the highly potassic calc-alkaline lavas from the central Andes were considered, thus excluding the average-level potassic suites from other segments of the arc.

For comparison with the granodiorite, the Andean average was calculated in the $60\% \leqslant SiO_2 \leqslant 68\%$ interval (Table 3) based on ~ 400 determinations for major elements and 100–400 determinations for trace elements, depending on the element. For many elements (Hf, Zr, rare earths in particular), this average shows low standard deviations (Table 3), which makes it possible to assign a representativity at the scale of the central Andes. The averages of the Andean rocks and the granodiorite show strong analogies, but also some differences concerning: (1) alkaline major elements—the granodiorite is generally more sodic ($Na_2O = 4.54\%$ compared to 3.78%) and less potassic ($K_2O = 2.66\%$ compared to 3.11%) than the andesite and dacite of the central Andes, (2) some trace or minor elements, such as Ba, Sr and Th, are more abundant in the granodiorite (Ba = 1205 ppm compared to 869 ppm, Sr = 703 ppm compared to 558 ppm, Th = 18 ppm compared to 13.9 ppm), whereas others, such as P and U, are less abundant in the granodiorite ($P_2O_5 = 0.24\%$ compared to 0.38%, U = 1.54 ppm compared to 4.16 ppm). It should nevertheless be noted that these elements give the highest standard deviation obtained on the Andean average (Table 3); their contents in the central Andean lavas thus vary the most. The most significant differences concern P and U, the latter reflecting a particularly high Th/U ratio in the granodiorite of the late Eburnean belt (~ 10 compared to 3 in the Andean average).

For comparison with the biotite granite, the Andean average was calculated in the $68\% \leqslant SiO_2 \leqslant 72\%$ interval (rhyodacite, dacite and granite), and the age range was broadened to the late Miocene so as to provide a sufficient statistical base (~ 80 determinations for major elements and 20–65 for trace elements, depending on the element) (Table 4). For calculation of the average for the biotite granite, the two 'extreme' samples (EE133 and EE64C) were not taken into account. Strong analogies are observed, as well as some notable differences relating to: (1) alkaline major elements—the biotite granite is generally richer in Na and K ($Na_2O = 4.45\%$ compared to 3.45% and $K_2O = 4.49\%$ compared to 4%), (2) trace elements,

such as Ba, Sr, Hf, Zr, and light rare earths are systematically more abundant in the biotite granite than in the rhyodacite and rhyolite of the central Andes (Ba = 1587 ppm compared to 665 ppm, Sr = 439 ppm compared to 360 ppm, Zr = 250 ppm compared to 155 ppm, La = 72 ppm compared to 35 ppm). These trace elements show fairly variable contents in the biotite granite of the late Eburnean belt.

For comparison with the monzogranite, the Andean average was calculated by only taking into account the most acid rocks (i.e. $SiO_2 > 70\%$) and for an age range extending to the late Miocene. Strong analogies are observed for the major elements and numerous trace elements (Rb, Ba, Sr, Hf, Zr, Sm, Tb). Conversely, the monzogranite of the late Eburnean belt is considerably richer in Th and light rare earths, but more depleted in U, Ta, Nb, Y and Yb.

The comparisons considered above reveal strong geochemical analogies between the granitic rocks of the late Eburnean plutonic belt and the recent calc-alkaline rocks of the central Andes, with nevertheless certain differences: (1) a particularly high Th/U ratio and low P contents in the granodiorite; (2) high Ba, Zr and light rare earth contents in the biotite granite; (3) high Th and light rare earth contents, but low Ta, Nb and Yb contents in the monzogranite.

These geochemical similarities (Figs. 8, 10 and 11) and the location of the late Eburnean belt along the margin of the Archean craton point strongly towards a relationship with plate convergence dynamics. Along similar lines, the generally acid and marked potassic nature of these granitic rocks may indicate major crustal participation, which is consistent with the location of the plutonic belt around the Archean craton. We can thus envisage that, at about 2090–2070 Ma, the margin of the Archean craton of West Africa constituted an active margin system where the magma was subjected to strong contamination from the Archean crust. Nevertheless, the strict application of an 'Andean model' poses various problems. Firstly, the late Eburnean events occurred over a very short time interval ($\leqslant 20$ Ma) and secondly, such a model does not take into consideration the peraluminous two-mica granite from the eastern edge of the Siguiri Basin. These granitic rocks, which may be derived from the partial melting of pelitic metasediments ('S-type' granite of Chappell and White, 1974), suggest that anatexis occurred beneath the outcropping Birimian domain.

In summary, the late Eburnean magmatism along the margin of the Archean craton in eastern Guinea includes at least two 'provinces' reflecting specific geodynamic situations, but induced by the same cause (oceanic subduction): (1) an active margin along the edge of the Archean craton; (2) a restricted anatectic domain involving aluminous sediments, slightly set aside from the active margin, below the Siguiri Basin.

7.3. Structural evolution of the belt: sinistral strike–slip along the northwestern margin of the Archean domain

The late Eburnean plutonic belt was emplaced and moulded in a subsolidus state around the edge of the Kénéma–Man craton. The belt was then affected by major sinistral strike–slip mylonitic shear zones that were formed under conditions ranging from subsolidus to clearly post-magmatic in many areas. However, these shear zones were active during formation of the granitic belt, after granodiorite emplacement but before monzogranite intrusion. The tectonic evolution of the late Eburnean belt is thus contemporaneous with its magmatic history, which highlights further the rapidity of events in this area. Sinistral transcurrent tectonism is mainly accommodated by the plutonic belt in a restricted area *located along*, *and parallel to*, the northwestern margin of the Archean domain. This domain represented a rigid block compared to the ductile-forming plutonic belt.

The location and dominant WNW–ESE orientation of the sinistral strike–slip faults make it possible to propose a late Eburnean deformation resulting from regional shortening towards the WSW, mainly accommodated by sinistral strike–slip along the northwestern margin of the Archean domain. Consequently, this northwestern margin can be considered as a major sinistral strike–slip zone of regional scale.

8. Conclusion

The new mapping and geochronological work carried out in eastern Guinea has revealed a major plutonic unit comprising granitic rocks of late Eburnean age that extends along the margin of the Archean Kénéma–Man craton. The magmatic and structural evolution of this belt took place over a relatively short time interval, namely c. 2090–2070 Ma. On the whole, the granitic rocks show strong geochemical analogies with the magmatic suites of recent active margins and, more precisely, with calc-alkaline rocks of the central Andes; there is evidence to suggest strong contamination from the Archean crust. These analogies make it possible to envisage the emplacement of the plutonic belt directly above a subduction zone. In such a context, the occurrence of peraluminous granite in the Siguiri Basin, at the northern extension of the plutonic belt, may suggest that the convergence here was associated with the local melting of metasedimentary rocks in the deep part of the basin.

Contemporaneously with its emplacement, the late Eburnean plutonic belt accommodated regional convergence by major WNW–ESE sinistral movements along the northwestern margin of the Archean block. A regional shortening towards the WSW is envisaged at the scale of eastern Guinea in relation with these kinematics.

The late Eburnean plutonic belt of eastern Guinea is a key element of the Archean/Proterozoic transition zone in southwest Africa. Evidence along the western and northwestern border of the Archean Kénéma–Man domain leads us to interpret this transition zone as an active margin, along which strike–slip tectonism accomodated regional convergence, towards the end of the Eburnean cycle.

Acknowledgements

This work forms part of two projects: the 1:200 000-scale geological mapping of northeastern Guinea sponsored by the World Bank, and the joint French-Guinean 1:200 000-scale mapping project of southeastern Guinea sponsored by the French Cooperation. Additional financial support was provided by the Scientific Direction of BRGM. A. Baldé, M. Bah, B. Diabaté, A. Diallo, A.B. Diallo, S. Diallo, F. Gaye, D. Minthé and H. Sané, all members of the National Guinean Direction of Geological and Hydrocarbon Research (DNRGH), are gratefully acknowledged for their collaboration and help in the field. Special thanks are due to G. Pézeril and I.S. N'Diaye who made these projects possible. The Guinean authorities are thanked for helping with the smooth running of the work in the field. The authors would like to thank Prof. J.D. Kramers and an anonymous reviewer for their criticism and suggestions, which greatly improved the paper. The authors are grateful to R. Stead for improving the English.

References

Abouchami, W., Boher, M., Michard, A., Albarède, F., 1990. A major 2.1 Ga old event of mafic magmatism in West Africa: an early stage of crustal accretion. J. Geophys. Res. 95, 17605–17629.

Barker, F., 1979. Trondhjemite: definition, environment and hypotheses of origin. In: Barker, F. (Ed.), Trondhjemites, Dacites and Related Rocks. In: Developments in Petrology, vol. 6. Elsevier, Amsterdam, pp. 1–11.

Beckinsale, R.D., Gale, N.H., Pankhurst, R.J., MacFarlane, A., Crow, M.J., Arthurs, J.W., Wilkinson, A.F., 1980. Discordant Rb–Sr and Pb–Pb whole rock isochron ages for the Archean basement of Sierra Leone. Precambrian Res. 13, 63–76.

Bering, D., Brinckmann, J., Camara, N., Diawara, M., Gast, L., Kieita, S., 1998. Evaluation de l'Inventaire des Ressources Minérales de Guinée. Coopération Technique République de Guinée—République Fédérale d'Allemagne, Projet 94.2025.8, BGR, Hannovre, p. 109.

Bessoles, B., 1977. Géologie de l'Afrique. Le Craton Ouest Africain. Mém. BRGM, 88, p. 420.

Billa, M., Feybesse, J.L., Bronner, G., Lerouge, C., Milési, J.P., Traoré, S., Diaby, S., 1999. Les formations à quartzites rubanés ferrugineux des Monts Nimba et du Simandou: des unités empilées tectoniquement, sur un « soubassement » plutonique Archéen (craton de Kénéma–Man), lors de l'orogène eburnéen. C.R. Acad. Sci. Paris Sci. Terre Planet 329, 287–294.

Boher, M., Abouchami, W., Michard, A., Albarède, F., Arndt, T.N., 1992. Crustal growth in West Africa at 2.1 Ga. J. Geophys. Res. 97, 345–369.

Bonhomme, M., 1962. Contribution à l'étude géochronologique de la plate-forme de l'Ouest africain.

Thèse. Ann. Fac. Sci. Univ. Clermond-Ferrand, Fr., Géol. Minéral 5, p. 62.

Briqueu, L., Bougault, H., Joron, J.L., 1984. Quantification of Nb, Ta, Ti and V anomalies in magmas associated with subduction zones: petrogenetic implications. Earth Planet Sci. Lett. 68, 297–308.

Cahen, L., Snelling, N.J., Delhal, J., Vail, J.R., 1984. The Geochronology and Evolution of Africa. Clarendon Press, Oxford, p. 512.

Camil, J., Tempier, P., Pin, C., 1983. Age libérien des quartzites à magnétite de la région de Man (Côte d'Ivoire) et leur place dans l'orogène libérien. C.R. Acad. Sci. Paris 296, 149–151.

Chappell, B.W., White, A.J.R., 1974. Two contrasting granite types. Pacific Geol. 8, 173–174.

Cocherie, A., Guerrot, C., Rossi, P., 1992. Single-zircon dating by step-wise Pb evaporation: comparison with other geochronological techniques applied to the Hercynian granites of Corsica. Chem. Geol. 101, 131–141.

Cocherie, A., Legendre, O., Peucat, J.J., Kouamelan, A., 1998. Geochronology of polygenetic monazite constrained by in situ electron microprobe Th–U–total Pb determination: implications for Pb behaviour in monazite. Geochim. Cosmochim. Acta 62, 2475–2497.

Deckart, K., Féraud, G., Bertrand, H., 1997. Age of Jurassic continental tholeiites of French Guyana, Surinam and Guinea: implications for the initial opening of the Central Atlantic Ocean. Earth Planet Sci. Lett. 150, 205–220.

Feybesse, J.L., Milèsi, J.P., 1994. The Archean/Proterozoic contact zone in West Africa: a mountain belt of décollement thrusting and folding on a continental margin related to 2.1 Ga convergence of Archean cratons? Precambrian Res. 69, 199–227.

Feybesse, J.L., Bangoura, A., Billa, M., Costea, C.A., Diabeté, B., Diaby, S., Diallo, A, Diallo, S., Diallo, A.B., Egal, E., Freyssinet, P., Gaye, F., Guerrot, C., Iliescu, D., Lacomme, A., Lahondère, D., Le Berre, P., Milési, J.P., Minthé, D., Soumah, D., 1999. BRGM, DNRGH. Notice explicative de la Carte géologique de la Guinée à 1/200 000, Feuille no. 19, Kankan. Conakry (GIN): Ministère des Mines, de la Géologie et de l'Environnement, 27 p.

Gaudette, H.E., Lafon, J.M., Macambira, M.J.B., Moura, C.A.V., Scheller, T., 1998. Comparison of single filament Pb evaporation/ionization zircons ages with conventional U–Pb results; examples from the Precambrian of Brazil. J. S. Am. Earth Sc. 11, 351–363.

Gill, J.B., 1981. Orogenic Andesites and Plate Tectonics. Springer, Berlin, p. 390.

Goloubinow, M.R., 1936. Géologie et ressources en or du Nord-Est de la Guinée. Thèse, Fac. Sci. Nancy p. 140.

Goujou, J.C., Thiéblemont, D., Delor, C., Cocherie, A., Lacomme, A., Lafon, J.M., Tegyey, M., Théveniaut, H., Sall, H., Souaré, S., Touré, J., Bah, M., Baldé, A., Sané, H., 1999. BRGM, DNRGH. Notice explicative de la Carte géologique de la Guinée à 1/200 000; Feuille no. 30, Macenta. Conakry (GIN): Ministère des Mines, de la Géologie et de l'Environnement. 22 p.

Hildreth, W., Moorbath, S., 1988. Crustal contributions to arc magmatism in the Andes of Central Chile. Contrib. Mineral. Petrol. 98, 455–489.

Hirdes, W., Davis, D.W., Eisenlohr, B.N., 1992. Reassessment of Proterozoic granitoid ages in Ghana on the basis of U/Pb zircon and monazite dating. Precambrian Res. 56, 89–96.

Hirdes, W., Davis, D.W., Lüdtke, G., Konan, G., 1996. Two generations of Birimian (Paleoproterozoic) volcanic belts in northeastern Côte d'Ivoire (West Africa): consequences for the "Birimian controversy". Precambrian Res. 80, 173–191.

Hofmann, A.W., 1988. Chemical differentiation of the Earth. The relationship between mantle, continental crust and oceanic crust. Earth Planet Sci. Lett. 90, 297–314.

Hurley, P.M., Leo, G.W., White, R.W., Fairbairn, H.W., 1971. Liberian age province (about 2700 My) and adjacent provinces in Liberia and Sierra Leone. Geol. Soc. Am. Bull. 82, 3483–3490.

Klötzli, U.S., 1997. Single zircon evaporation thermal ionisation mass spectrometry: method and procedure. Analyst 122, 1239–1248.

Kober, B., 1986. Whole grain evaporation $^{207}Pb/^{206}Pb$-age—investigation on single zircons using a double filament thermal ion source. Contrib. Mineral. Petrol. 93, 482–490.

Kober, B., 1987. Single zircon evaporation combined with Pb^{+} emitter bedding for $^{207}Pb/^{206}Pb$-age investigations using thermal ion mass spectrometry and implications for zirconology. Contrib. Mineral. Petrol. 96, 63–71.

Kouamelan, A.N., Delor, C., Peucat, J.J., 1997. Geochronological evidence for reworking of Archean terrains during the Early Proterozoic (2.1 Ga) in the western Côte d'Ivoire (Man Rise-West African Craton). Precambrian Res. 86, 177–199.

Lahondère, D., Lacomme, A., Le Berre, P., Iliescu, D., Guerrot, C., Cocherie, A., Diabaté, B., Gaye, F., Thiéblemont, D., Minthé, D., Feybesse, J.L., 1999. BRGM, DNRGH. Notice explicative de la Carte géologique de la Guinée à 1/200 000, Feuille no. 27–28, Damaro-Odienné. Conakry (GIN): Ministère des Mines, de la Géologie et de l'Environnement, 22 pp.

Lahondère, D., Thiéblemont D., Tegyey M., Guerrot C., Diabaté, B., The first evidence of Pre-Birimian volcanic and associated rocks of the Niani suite. J. Af. Earth Sci., in press-a.

Lahondère, D., Thiéblemont, D., Tegyey, M., Guerrot, C., Diabaté, B., in press. First evidence of Early Birimian volcanic activity in Upper Guinea: the volcanics and associated rocks of the Niani suite. J. Af. Earth Sci., in press-b.

Lamotte, M., Routhier, P., 1943. Monographie géologique du Mont Nimba. Contribution à l'étude du Birrimien d'A.O.F. Bull. Soc. géol. France 5 (XIII), 113–124.

Ludwig, K.R., 1999. Isoplot/Ex version 2.06: A Geochronological Toolkit for Microsoft Excel. Berkeley Geochronology Center, Special Publication No. 1a. p. 49.

MacFarlane, A., Crow, M.J., Arthurs, J.W., Wilkinson, A.F., Ancott, J.W., 1981. The geology and mineral resources of

Northern Sierra Leone. Overseas Mem. 7. Inst. Geol. Sci., London, p. 103.

Milési, J.P., Feybesse, J.L., Ledru, P., Dommanget, A., Ouedraogo, M.F., Marcoux, E., Prost, A., Vinchon, C., Sylvain, J.P., Johan, V., Tegyey, M., Calvez, J.P., Lagny, P.H., 1989. West African gold deposits in their Lower Proterozoic lithostructural setting. Chron. Rech. Min. 497, 3–98.

Mittlefehldt, D.W., Miller, C.F., 1983. Geochemistry of the Sweetwater Wash Pluton, California: implications for « anomalous » trace element behavior during differentiation of felsic magmas. Geochim. Cosmochim. Acta 47, 109–124.

Miyashiro, A., 1974. Volcanic rock series in island-arcs and active continental margins. Am. J. Sci. 274, 321–355.

Obermüller, A., 1941. Description pétrographique et étude géologique de la région forestière de la Guinée française. Bull. Serv. Mines A.O.F. 5, 207.

Obermüller, A., Roques, M., 1946. Discordance de la Série antécambriene du Simandou sur les Gneiss de Guinée (A.O.F.). C.R. Acad. Sci. Paris 223, 1163–1164.

Oberthür, T., Vetter, U., Davis, D.W., Amanor, J.A., 1998. Age constraints on gold mineralization and Paleoproterozoic crustal evolution in the Ashanti belt of southern Ghana. Precambrian Res. 89, 129–143.

O'Connor, J.T., 1965. A classification for quartz-rich igneous rocks based on feldspar ratios. US Geol. Surv. Prof. Pap. 525-B, 79–84.

Stacey, V.S., Kramers, J.D., 1975. Approximation of terrestrial lead isotope evolution by a two-stage model. Earth Planet Sci. Lett. 26, 207–221.

Thiéblemont, D., 1999. Discrimination entre magmatismes calco-alcalins mantellique et crustal: l'exemple des Andes. C.R. Acad. Sci. Paris, Sci. Terre Planet 329, 243–250.

Thiéblemont, D., Tegyey, M., 1994. Une discrimination géochimique des roches différenciées témoin de la diversité d'origine et de situation tectonique des magmas calco-alcalins. C.R. Acad. Sci. Paris 319 (II), 87–94.

Thiéblemont, D., Delor, C., Goujou, J.C., Lacomme, A., Cocherie, A., Lafon, J.M., Tegyey, M., Théveniaut, H., Bah, M., Baldé, A., Sané, H., 1999. Notice explicative de la Carte géologique de la Guinée à 1/200 000; Feuille no. 31–32, Beyla-Touba. Conakry (GIN): Ministère des Mines, de la Géologie et de l'Environnement, 21 pp.

Thiéblemont, D., Delor, C., Cocherie, A., Lafon, J.M., Goujou, J.C., Baldé, A., Bah, M., Sané, H., Fanning, M.A., 2001. 3.5 ga granite-gneiss basement in Guinea: further evidence for early Archean accretion within the west african Craton. Precambrian Res. 108, 179–194.